Structural Chemistry, Flexibility and CO_2 Adsorption Performance of Alkali Metal Forms of Merlinoite with Framework Si/Al Ratio of 4.2

Elliott L. Bruce,[1] Veselina M. Georgieva,[1] Maarten C. Verbraeken,[2] Claire Murray,[3] Ming-Feng Hsieh,[4] William J. Casteel, Jr.,[5] Alessandro Turrina,[4] Stefano Brandani[2] and Paul A. Wright[1,*]

1. EaStCHEM School of Chemistry, University of St Andrews, Purdie Building, North Haugh, St Andrews, UK.

2. School of Engineering, University of Edinburgh, The King's Buildings, Edinburgh, UK

3. Diamond Light Source, Harwell Science and Innovation Campus, Didcot, UK

4. Johnson Matthey Technology Centre, Chilton P.O. Box 1, Belasis Avenue, Billingham, UK

5. Air Products and Chemicals Inc., 7201 Hamilton Blvd., Allentown, PA18195 USA

***** *email: paw2@st-andrews.ac.uk*

Abstract

Small pore zeolites that show framework flexibility, such as merlinoite (topology type MER), possess high potential for the selective adsorption of small gas molecules including CO_2. The CO_2 adsorption properties of Na-, K- and Cs-exchanged forms of a merlinoite zeolite with Si/Al = 4.2 have been measured at 298 K and *in situ* PXRD used to follow their structural response to dehydration and CO_2 uptake. The Na- and Cs- forms convert from a wide-pore to a narrow-pore form upon dehydration, while the K-form remains in the wide-pore form. The Na- and Cs-forms exhibit stepped CO_2 adsorption isotherms, consistent with breathing behaviour and expansion from narrow- to wide-pore phases, whilst $K_{6.2}$-MER remains in the wide-pore structure throughout. Synchrotron PXRD of the K- and Cs-forms reveals the effects of CO_2 adsorption on the cation site distributions and the framework configuration. All cation forms of MER (4.2) show enhanced adsorption kinetics for Ar compared to those with lower Si/Al and the wide-pore structure of $K_{6.2}$-MER (4.2) shows particularly rapid sorption for both Ar and CO_2. Breakthrough curves over $K_{6.2}$-MER(4.2) demonstrate good separation of CO_2 from CH_4 in flowing CO_2/CH_4 mixtures, even in pelletised form with an alumina binder.

Introduction

Porous materials exhibit a diverse range of applications including catalysis, ion exchange and gas adsorption.[1–3] The threat of global warming and climate change posed by increased CO_2 levels provide an impetus for the development of green technologies, including gas separation processes with porous materials,[4–6] such as carbon capture from industrial sources.[7] This may involve pre- or post-combustion uptake of CO_2 to reduce the environmental impact of fossil fuel infrastructure, landfills or biogas usage.[8–11] Zeolites are a promising family of porous materials for such processes,[12] due to their adsorption properties and high thermal and hydrolytic stability.[13]

Small pore zeolites, such as zeolite A (framework type LTA), chabazite (CHA) and Rho (RHO), are amongst those with potential for gas separation processes such as CO_2 over CH_4.[14–19] High CO_2 selectivity over CH_4 in pre-combustion biogas upgrading as well as over N_2 in post-combustion flue gas purification has been reported in zeolite A.[20,21] This is also the case for chabazite and ZK-5.[12,15,22] The 8-membered rings (8Rs) within these structures allow for adsorption of small gas molecules, while facilitating kinetic separation or molecular sieving. Very narrow 8R windows, however, can slow the rate of adsorption of desired molecules and thus limit application, so that a successful CO_2 adsorbent should have sufficiently wide 8R windows for rapid CO_2 diffusion, but not so large as to compromise molecular sieving.

Zeolite merlinoite (MER) is a promising candidate for carbon capture. It comprises *d8r*, *pau* and *ste* cages, with the cavity types and extended framework shown in Figure 1: 8Rs define channels along all three axes. MER possesses a flexible framework which distorts upon dehydration to coordinate extra-framework cations more closely. Recently we reported the modification of this distortion in a MER material with Si/Al = 3.8, by adjusting univalent cation content (Na, K and Cs).[23] Larger cations reduced the distortion of the structure, with wider 8R windows. We also observed "breathing" effects, with the framework expanding upon CO_2 adsorption *via* a narrow- to wide-pore transition. The pressure at which the transition occurs depends on the type of cations present; K-MER (3.8) showed the lowest opening pressure and kinetic adsorption measurements identified this form as the most promising for CO_2/CH_4 separations. We attributed this behaviour to a combination of cation siting

preferences and framework distortion effects directed by K cations. Recent work by Choi *et al*. reported similar behaviour in MER materials, including materials with Si/Al = 2.3.[24]

We have since obtained a merlinoite with a slightly higher Si/Al ratio (4.2). The cation content

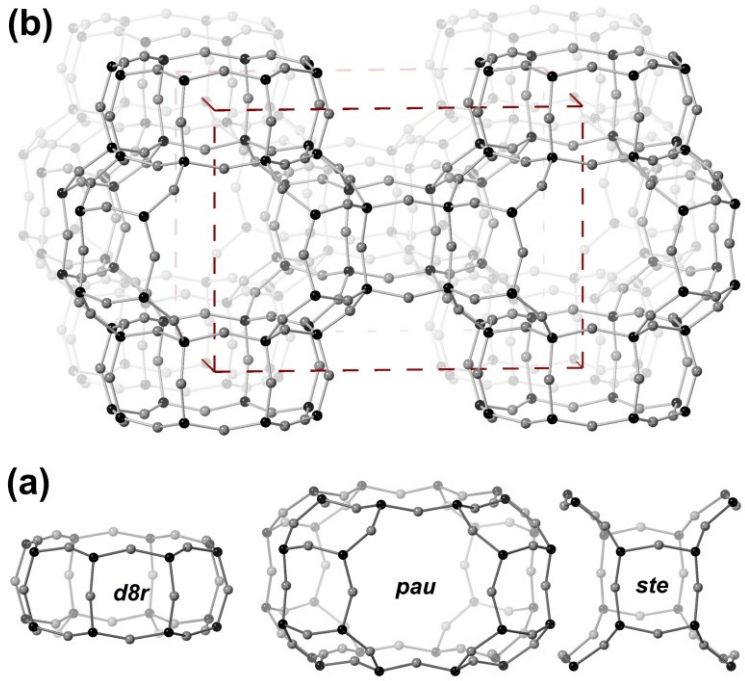

Figure 1. Structural representations of zeolite merlinoite. (a) Cavity types present in MER and (b) open framework structure of MER. Tetrahedral cation sites and O sites are shown in black and grey, respectively. The unit cell is indicated by a dashed red line.

per unit cell is correspondingly reduced from 6.7 to 6.2 per unit cell. Recently we reported that this had enabled us to produce a Li-MER sample, previously found to be unstable to dehydration in the Si/Al = 3.8 material.[25] For the Na, K and Cs forms, this small reduction in cation content has a significant effect on their equilibrium and kinetic properties of CO_2 adsorption and CO_2/CH_4 separation. In situ powder X-ray diffraction (PXRD) enables the structural changes associated with the CO_2 adsorption behaviour to be related to the cation type and location. For the most promising adsorbent, K-MER (4.2), the material has been prepared in bead form with an alumina binder and the properties of the composite measured.

Methods

Exchange of MER Zeolites

K,TEA-MER (TEA= tetraethylammonium) with a Si/Al ratio of 4.2 was provided by Johnson Matthey. SEM images are given in Figures S1.1-1.2. The as-prepared K,TEA-MER was heated at 823 K under oxygen for 12 h to remove the template (K,H-MER). The calcined zeolite was repeatedly exchanged with 10% nitrate solutions of Na, K and Cs (99.5-99.9%; Sigma-Aldrich) at 353 K in a round bottom flask with a condenser. In all cases, cation exchange was repeated until EDX analysis indicated the exchange was complete. The binary $K_{6.2-x}Na_x[Al_{6.2}Si_{25.8}O_{64}]$ series, where x is close to the integer values 1-6, was prepared from 0.3 g of K-MER, stirred in 200 mL of different concentrations of sodium nitrate solution at 378 K for 5 h. All ion exchanged samples were washed with deionised water and dried overnight at 378 K prior to any characterisation. EDX analysis of all samples was performed in a JEOL JSM 5600 SEM with an Oxford INCA Energy 200 EDX analyser.

Pelletisation

9.8 g of Catapal A alumina hydrate was added to 17.9 g of $K_{6.2}$-MER to generate a powder mixture. The powder mixture was then transferred to a Brabender® mixing torque rheometer for paste formation, where a suitable amount of water was added at a constant rate during kneading to give a paste with plasticity. The paste was transferred to a Caleva 3-in-1 Multi Lab for extrusion, where an extrusion rate of 100 rpm and a 1.6 mm die with 1 mm depth were applied. The extrudates were subsequently moved to the spheroniser of the same Caleva 3-in-1 Multi Lab unit, where 3000 rpm rotation speed was employed for 1 – 2 mins to make alumina-bound MER granules by breaking extrudates. The obtained granules were oven dried at 383 K overnight and sieved with a range of sizes. Prior to measurement of breakthrough properties the sample was heated at 573 K for 16 h in helium.

Sorption Isotherms

CO_2 adsorption isotherms were measured volumetrically for all samples at 298 K from 0 to 1 bar using a Micromeritics ASAP 2020 Gas Adsorption Analyzer connected to a Julabo F25 Chiller Unit. The samples were heated to 363 at 5 K min^{-1} under vacuum and held for 1 h before being heated to 523 K under vacuum at 5 K min^{-1} and held at this temperature for 6 h before cooling and measurement. At each adsorption or desorption step the pressure was

sampled every 7 s until no further change is observed, so that step times ranged from 10 to 100 min.

High-pressure CO_2 adsorption isotherms were measured from 0 to 5 bar at 298 K using a Hiden IGA gravimetric analyser using ~20 mg of sample, which was outgassed at 573 K under vacuum for 10 h before each adsorption experiment. The temperature of the sample was subsequently reduced under vacuum until the target temperature (between 298 and 328 K) was reached. The mass change for each adsorption/desorption step was followed, and a final reading was taken when it had reached 98% of the asymptotic equilibrium value or after 90 min, whichever was shorter.

Sorption Kinetic Analysis

Zero Length Column (ZLC) experiments were performed to assess the kinetics of CO_2 sorption. The ZLC technique and experimental apparatus are described in detail in refs.[26–29] In summary, a small amount (5 – 10 mg) of merlinoite sample was packed into a 1/8" stainless steel union (Swagelok®), fitted with two porous metal discs to keep the powder in place. The determination of the diffusional time constant using the ZLC experiment the analysis is independent of the sample mass, provided that a sufficiently small sample is used so that the "zero-length" approximation is valid. For CO_2 on cationic zeolites 5-10 mg is the correct range of sample mass.[29] The column and gas connections are placed within an oven (Carbolite) with thermostatic control (Eurotherm) or alternatively inside a cooling jacket, connected to a thermostatic bath for temperature control (Julabo F-25). The pure helium carrier and dosing gas mixtures (typically 1 – 10 vol.% CO_2 in helium) are supplied through mass flow controllers (Brooks Instrument) and a combination of four solenoid valves is used to direct either of the two gas streams to the ZLC. Both helium (BOC, CP grade, 99.999% purity) and CO_2 (BOC, 99.8% purity) are additionally dried using columns packed with a combination of silica gel and zeolite 5A molecular sieve. The gas leaving the ZLC is analysed by mass spectrometry (Dycor Residual Gas Analyzer, Ametek Process Instruments). Prior to ZLC measurements, the samples were activated overnight at 523 K ($Na_{6.2}$-, $Cs_{6.2}$-MER) or 573 K ($K_{6.2}$-MER) under a flow of helium. The as-received signals were corrected to account for effects which are intrinsic to the experimental setup, by means of a deconvolution procedure as described in Verbraeken *et al*.[30] This procedure yields the concentration of the gas as it leaves the column and removes extra-column contributions, such as those arising from the detector.

The materials' potential for gas separation was tested *via* breakthrough experiments. These were carried out in a gas mixture which is taken as representative for CO_2-containing natural gas, with a composition 10% CO_2 / 40% CH_4, balance He. In these experiments, a special "elongated" version of the zero length column (E-ZLC) was used, which consists of a Swagelok 1/8″ bulkhead union with an internal diameter of 2.286 mm and a length of 25.9 mm. The columns can hold up to three times the amount of sample that is normally used in a typical ZLC experiment, allowing for clear identification of the separation performance. Apart from the extended column, the experimental apparatus used for this study is the same as the Zero Length Column (ZLC) setup described above.[28] These measurements were performed on $Na_{6.2}$-, $K_{6.2}$- and $Cs_{6.2}$-MER in powder form. To study the effect of pelletisation on the separation performance, $K_{6.2}$-MER beads of varying size were measured in a similar way.

The multicomponent breakthrough experiments were carried out at 308 K at ambient pressure and at different flow rates, *i.e.* 1, and 2 mL min^{-1}. Prior to the experiments, 30 – 60 mg of each of the samples were activated overnight as for the ZLC measurements. The experiments consist of equilibrating the sample in a constant flow rate of the feed mixture. Once equilibrium is reached, the flow is switched to pure He, and the desorption starts. For the entire duration of the experiment, the gas composition is monitored using the mass spectrometer connected at the outlet of the column. To enable analysis of the results, blank runs were also carried out. These consist of repeating the breakthrough experiments under the same conditions as described above, but without adsorbent. In this case the column is filled with 2 mm glass beads to give a pressure drop and void fraction close to that observed in the presence of the samples. This allows the dead volume and the intrinsic kinetics of the system to be measured when no adsorption occurs.

The mass transfer properties of CO_2 in K-MER materials were qualitatively evaluated using a volumetric adsorption apparatus capable of rapidly logging absolute pressure. The experiment consisted of exposing *ca*. 2 g of an evacuated, activated adsorbent sample at 303 K to specific volumes of CO_2 at 300 Torr (40 kPa, 0.4 bar) and 380 Torr (51 kPa, 0.5 bar) for $K_{6.2}$-MER (4.2) and $K_{6.7}$-MER (3.8), respectively. The change in pressure was then followed as a function of time. The pressure/time data is then subtracted from a similar pressure history using the same weight of quartz beads in the place of the adsorbent sample to obtain a plot of the amount of gas adsorbed as a function of time or uptake curve. Heat dissipation from the adsorbent due to this relatively large pressure step change upon adsorbing CO_2 will significantly affect the diffusion parameter, so no attempt was made to extract the diffusion parameters from these

uptake curves. Relative rates of adsorption for CO_2 on the various MER samples were obtained by comparison of the plotted uptake curves.

The same volumetric adsorption unit was used to quantitatively evaluate the mass transfer properties of the Na-, K-, and Cs-exchanged forms of MER(3.8) and MER(4.2) for Ar. The experiment consisted of exposing *ca*. 2 g of an evacuated, activated adsorbent sample at 303 K, to specific volumes of Ar at 760 Torr (101 kPa). The change in pressure was then followed as a function of time to obtain an uptake curve, as above. From the initial slope of the uptake curve, a diffusion parameter for Ar in units of inverse time (s^{-1}) can be obtained. Because the heats of adsorption for argon on the MER adsorbents are relatively low, the diffusional parameter calculated under the assumption of isothermal behaviour should be a reasonable estimate of the diffusion parameter.

PXRD Analysis and Crystallography

Powder X-ray diffraction (PXRD) patterns of all single cation MER samples were measured at 298 K in the hydrated and dehydrated forms. The sample was loaded into a 0.7 mm quartz glass capillary to a depth of around 1 cm and a quartz wool plug was packed above this to prevent loss of powder upon evacuation and dehydration. Materials were analysed by synchrotron X-ray diffraction at I11 (λ = 0.826398 Å) at Diamond Light Source, Oxfordshire using a Mythen position sensitive detector. The samples were dehydrated under evacuation (10^{-5} mbar) for 1 – 2 h using an Oxford Cryocool blowing hot air at 500 K plus intermittent use of a hot air blower. The powder X-ray diffraction patterns of all hydrated and dehydrated samples were measured at I11, except for $K_{5.2}Na_{1.0}$-, $K_{4.2}Na_{2.0}$- and $K_{2.2}Na_{4.0}$-MER which were analysed in Debye−Scherrer geometry on a Stoe STAD i/p diffractometer using Cu $K_{\alpha 1}$ X-rays (1.54056 Å). For these materials, powders were loaded into 0.7 mm quartz glass capillaries to a depth of around 2 cm and heated for 16 h at 623 K under a vacuum of 10^{-5} mbar on a glass line. After full dehydration of these materials, all capillaries were flame sealed under vacuum.

To observe the structural changes during CO_2 adsorption on MER samples, *in situ* X-ray powder diffraction was performed on a PANalytical Empyrean diffractometer with a Mo X-ray tube with a ß-filter (giving Mo $K_{\alpha 1,2}$ X-rays) and an X'celerator RTMS detector. The instrument was equipped with an Anton Paar HTK1200N stage (operating range, room temperature to 1100 K, up to 1 bar of inert/reducing gas), working in reflection, Bragg−Brentano, θ−θ mode. First, the sample was placed on an alumina disk and inserted in a cell, equipped with a furnace. The sample was evacuated and degassed at 573 K for 8 h under

a vacuum of 10^{-6} mbar. The furnace was attached to a gas handling rig and CO_2 was dosed *via* a needle valve. The pressure was followed on a RS PRO vacuum gauge with a maximum pressure measurement of 0 bar overpressure (1 bar pressure). Series of diffraction patterns, each of 60 min and over the 2θ range 3.5−25°, were collected at 298 K before and after dehydration and also after dosing with 0.02, 0.10, 0.20, 0.30, 0.40, 0.60, 0.70, 0.80, and 1.0 bar CO_2, each time after 30 min equilibration.

The structural response to CO_2 adsorption of pure cation MER forms was also measured at I11 at the Diamond Light Source (0.826398 Å). For each sample, a capillary was attached to a gas dosing line attached to a goniometer head, which was permitted to rock by 20° in the beam to improve powder averaging during diffraction. The sample was dehydrated as previously described. Series of diffraction patterns, each of 2 minutes and over the 2θ range 2 – 90°, were collected at 298 K before and after dehydration, and also after dosing with CO_2, each time after 10-20 minutes equilibration. Measurements were made using the Mythen position sensitive detector. This gave excellent signal to noise in very short collection times and is the detector of choice for these measurements on our samples. The pressure of CO_2 was increased stepwise from 0.02 to 5 bar, and then removed by evacuation, either fully or in some cases partially, to measure the isotherms on the desorption branch of the isotherm.

Structures were determined by Rietveld refinement against PXRD data using TOPAS Academic software.[31] Starting framework models were adapted from literature examples with the unit cell modified to that derived from the diffraction pattern. For dehydrated materials, the *Pmmn* space group gave the best fits in most cases, with some samples best fitted by the *Immm* space group. Starting cation positions were estimated from literature models, and geometric restraints on T−O and O−O distances of 1.63 and 2.66 Å, respectively, were used to maintain regular tetrahedral coordination. Pseudo-Voigt peak profiles gave the best fit of those available. Final extra-framework cation positions and occupancies were determined by refinement of starting positions and through the use of difference Fourier mapping. The latter was used to determine the positions of water and CO_2 molecules in hydrated and CO_2-loaded samples, respectively. Water molecules were modelled as a single O atom whilst CO_2 molecules were treated as rigid bodies, with final positions and occupancies determined by refinement. Further details on Rietveld refinement are given in the Supporting Information.

Results & Discussion

Structures of MER (4.2)

Previously we reported the synthesis of various cation forms of a zeolite merlinoite (MER) with Si/Al = 3.8.[23] Altering the cation content of this material strongly affected the adsorption properties, according to the size and siting of Na, K and Cs cations. Here, we investigate a material with Si/Al = 4. 2, with correspondingly fewer cations in the structure (6.2 per unit cell (uc), as opposed to 6.7). To investigate the effect of reducing the number and locations of cations on the gating and breathing behaviour, and the impact on equilibrium and kinetic adsorption performance, $Na_{6.2}$-, $K_{6.2}$- and $Cs_{6.2}$-MER materials were prepared as described in the experimental section and their XRD patterns in hydrated and dehydrated forms are shown in Figure 2. (From here onwards all materials discussed have Si/Al = 4.2, unless stated otherwise.)

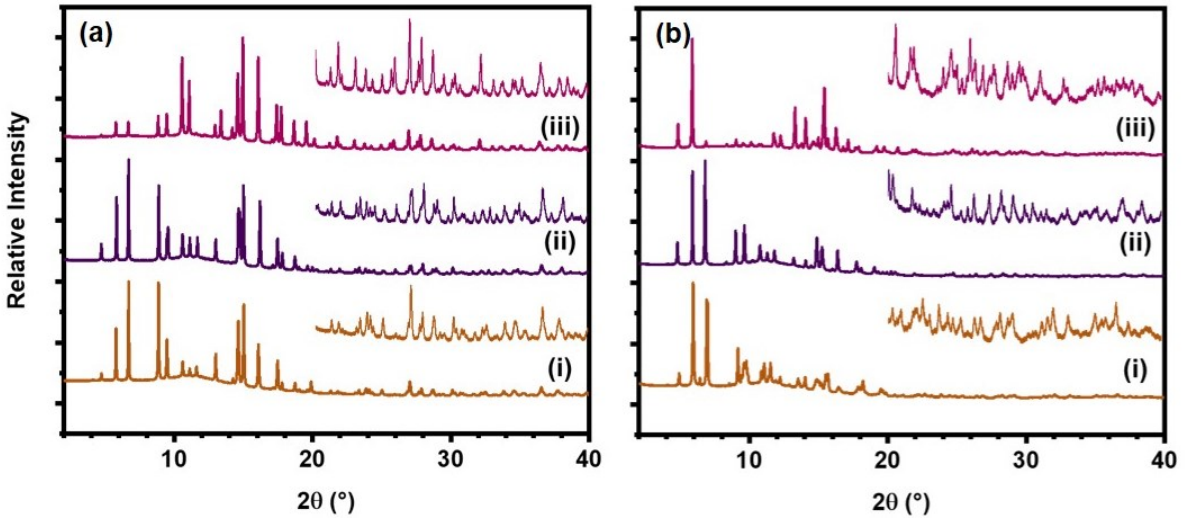

Figure 2. Synchrotron PXRD patterns of (a) hydrated and (b) dehydrated MER samples (λ = 0.826398 Å): (i) $Na_{6.2}$-, (ii) $K_{6.2}$- and (iii) $Cs_{6.2}$-MER.

Hydrated materials are all single phase. Upon dehydration their unit cells undergo contraction. As seen in Figure 2(b,i), Na-MER exhibits an additional peak at *ca*. 6.5° upon dehydration, and so far, the unit cell and space group of this phase has not been determined. However, as described below, a Na-MER with a small amount of K exchanged in has similar structure and properties to the Na-MER and can usefully be compared.

Rietveld refinement of K- and Cs-MER shows both adopt the *Pmmn* space group, a daughter space group of the $P4_2/nmc$ unit cells observed for the lower Si/Al analogues.[23] The unit cells

of these materials are very similar in appearance to those of the lower silica (Si/Al = 3.8) materials although the loss of tetragonal symmetry allows the *a* and *b* axis lengths to diverge and cation ordering to change. While $K_{6.2}$-MER can be fitted in $P4_2/nmc$ with little impact on the R_{wp} value, we consider that the improvement in peak profile fitting is consistent with distortion away from tetragonal to a pseudo-tetragonal system. The loss of the 4_2 axis also sees 2 separate sites (I and I') close to the *d8r* unit with different displacements from the S8R site. (An alternative fit using the higher symmetry space group is provided in S2.1.1). Crystallographic data is listed in Table 1 with extra details given in Section S2.

To compare cation locations in MER (4.2) with those in MER (3.8), when the symmetry is different (orthorhombic *Pmmn* compared to tetragonal $P4_2/nmc$) required alteration to the site labelling scheme we used previously. The revised nomenclature is illustrated in Figure 3. Those found in the planar 8Rs of the *pau* cavity are denoted as sites I and I'. For simplicity, and to aid discussion, these are treated together as site I*, more similar to site I in the Si/Al = 3.8 material. Cations in the centre of the *d8r* unit (Ia) and in the buckled 8Rs between *pau* and *ste* cavities (IIa and IIb, along *a* and *b* axes, respectively) retain previous labelling. Cations occupying the 2 symmetry inequivalent *ste* cavities are denoted by III and III', which are discussed together as III*. The nomenclature adopted for cation sites (I, II, III) is also used for associated 8R windows (I, *pau* cavity windows along [001]; II(a,b), between *pau* and *ste* cages; III, between ste cages; with I' and III' used for symmetry inequivalent relatives).

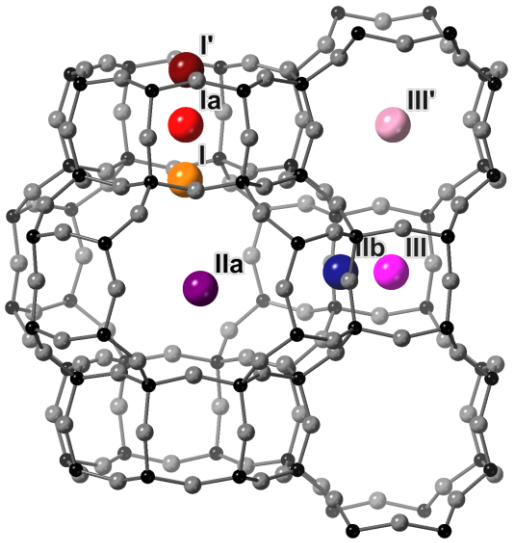

Figure 3. Open framework structure of MER with labelling schemes used here for cation sites. Tetrahedral cation sites and O sites are shown in black and grey, respectively. Extra-framework cation sites are shown as: I and I' (together termed I for ease), S8Rs between d8r and pau (orange and dark red); Ia, D8R (bright red); IIa and IIb (II*), S8R between pau and ste cavities (purple and blue); III and III' (III*), inside the ste cavity (bright and pastel pink).*

Table 1. Rietveld refinement details of dehydrated MER (4.2) samples, including space group (SG), unit cell parameters and R_{wp}.

Sample	Diffractometer	SG	*a* (Å)	*b* (Å)	*c* (Å)	*V* (Å^3)	R_{wp}
$Cs_{6.2}$-MER	I11	*Pmmn*	13.794(1)	13.776(1)	9.940(1)	1889(1)	5.5
$K_{6.2}$-MER	I11	*Pmmn*	13.950(1)	13.894(1)	9.831(1)	1905(1)	2.4
$K_{5.7}Na_{0.5}$-MER	I11	*Pmmn*	13.978(1)	13.913(1)	9.820(1)	1910(1)	3.3
$K_{5.2}Na_{1.0}$-MER	Stoe	*Pmmn*	13.918(1)	13.746(1)	9.862(1)	1887(1)	6.1
$K_{4.2}Na_{2.0}$-MER	Stoe	*Pmmn*	13.753(1)	13.647(1)	9.851(1)	1849(1)	5.7
$K_{3.2}Na_{3.0}$-MER	I11	*Pmmn*	13.671(1)	13.598(1)	9.864(1)	1833(1)	3.3
$K_{2.2}Na_{4.0}$-MER	Stoe	*Pmmn*	13.629(1)	13.564(1)	9.846(1)	1820(1)	5.8
$K_{1.2}Na_{5.0}$-MER	I11	*Pmmn*	13.606(1)	13.551(1)	9.845(1)	1815(1)	3.4

The structures of dehydrated $K_{6.2}$- and $Cs_{6.2}$-MER are shown in Figure 4, with site occupancies according to the nomenclature of Figure 3. Cation siting preferences were previously found to have important effects on adsorption properties and simplified details on site occupancies for these materials are given in Table 2, with a fuller description detailed in the Table S2.2.

*Table 2. Cation site distribution determined by Rietveld refinement. Site labelling (I, Ia, IIa, IIb, III) is largely as described in the text. Sites denoted by * indicate merging of related sites in Immm and $P4_2/nmc$ space groups, i.e. I, I' and III, III'. For each sample the multiplicity (M), fractional occupancy and number of cations per unit cell are given.*

Sample	I*			IIa			IIb		
	M	frac. occ.	atoms/uc	M	frac. occ.	atoms/uc	M	frac. occ.	atoms/uc
$K_{6.2}$-MER	4	0.31(1) K	1.2(1) K	4	0.58(1) K	2.3(1) K	4	0.64(1) K	2.6(1) K
$K_{5.7}Na_{0.5}$-MER	4	0.26(1) K	1.0(1) K	4	0.47(1) K	1.9(1) K	4	0.61(1) K	2.4(1) K
$K_{5.2}Na_{1.0}$-MER	4	0.41(2) K	1.6(1) K	4	0.37(1) K	1.5(1) K	4	0.78(1) K	3.1(1) K
$K_{4.2}Na_{2.0}$-MER	4	0.20(1) K	0.8(1) K	4	0.41(1) K	1.6(1) K	4	0.46(1) K	1.8(1) K
$K_{3.2}Na_{3.0}$-MER	4	0.38(2) Na	1.5(1) Na	4	0.37(1) K	1.5(1) K	4	0.38(1) K	1.5(1) K
$K_{2.2}Na_{4.0}$-MER	4	0.30(2) Na	1.2(1) Na	4	0.40(1) K	1.6(1) K	4	0.70(1) Na	2.8(1) Na
$K_{1.2}Na_{5.0}$-MER	4	0.38(3) Na	1.5(1) Na	4	0.31(1) K	1.2(1) K	4	0.66(2) Na	2.6(1) Na
Sample	**Ia**			**IIa**			**III***		
	M	frac. occ.	atoms/uc	M	frac. occ.	atoms/uc	M	frac. occ.	atoms/uc
$Cs_{6.2}$-MER	2	0.80(1) Cs	1.6(1) Cs	4	0.37(1) Cs	1.5(1) Cs	4	0.69(1) Cs	2.8(1) Cs

In $Cs_{6.2}$-MER, the *d8r* site has the highest fractional occupancy, whilst most cations are in sites in the *ste* cavities, as was observed in the lower silica, Si/Al = 2.3 and 3.8 materials.[23,24] $K_{6.2}$-MER has increased occupancy of window sites between *ste* and *pau* cavities compared to the Si/Al = 3.8 material (although lower than in the Si/Al = 2.3 analogue, due to the high cation

content of that material), and windows between neighbouring *ste* cavities are not occupied at this cation loading. Additional comparisons can be made of unit cell volumes, detailed in Table 1 and shown graphically in Figure 6. While the unit cell volumes of the Cs-MER materials are very similar (1874, 1881 and 1889 $Å^3$ in the Si/Al = 2.3, 3.8 and 4.2 materials, respectively), those of the K-MER analogues are very different. Whilst the lower silica materials have unit cell volumes of 1765 $Å^3$ (Si/Al = 2.3) and 1823 $Å^3$ (Si/Al = 3.8), in this material 1906 $Å^3$ is observed. This is closer to the wide-pore form previously observed and indeed the relative cation occupancies and diameters of windows are more in line with those seen in the expanded forms of $K_{6.7}$-MER (3.8). Hence, we see that the structure of $K_{6.2}$-MER remains in the wide-pore form upon dehydration.

To understand the effect of Na^+ cations on the unit cell of K-MER materials, a $K_{6.2-x}Na_x$-MER series was prepared. This showed that upon increased Na^+ content, the unit cell volume decreased from 1906 $Å^3$ for $K_{6.2}$-MER to 1815 $Å^3$ for $K_{1.2}Na_{5.0}$-MER, as shown in Figure 5(a). The structure of $Na_{5.0}K_{1.2}$-MER is illustrated in Figure 4(A). Notably, an *Immm* fit to the dehydrated $Na_{6.2}$-MER data suggests a unit cell volume of 1807 $Å^3$, in line with the gradual decrease in unit cell going from the K- to the Na-form, although it does not describe the additional peak at low angles. The reduction in the unit cell volume is accompanied by a decrease in the window size, as detailed in Table 3 and depicted in Figure 5(b). The mean free diameter of windows (narrowest distance across centre of 8R, less 2 O van der Waals radii, as described previously for MER (3.8) materials)[23] drops from 3.1 to 2.2 Å from $K_{6.2}$- to $K_{1.2}Na_{5.0}$-MER. Window shapes of materials with more than 1 Na^+/uc change from the "egg-shaped" *pau*/*ste* 8Rs to elliptical 8Rs as previously seen in $Na_{6.7}$-MER.[23] This is possible as the *Pmmn* space group is a daughter space group of both $P4_2/nmc$ and *Immm* space groups seen previously in the Si/Al = 3.8 materials for large and small cation forms, respectively.

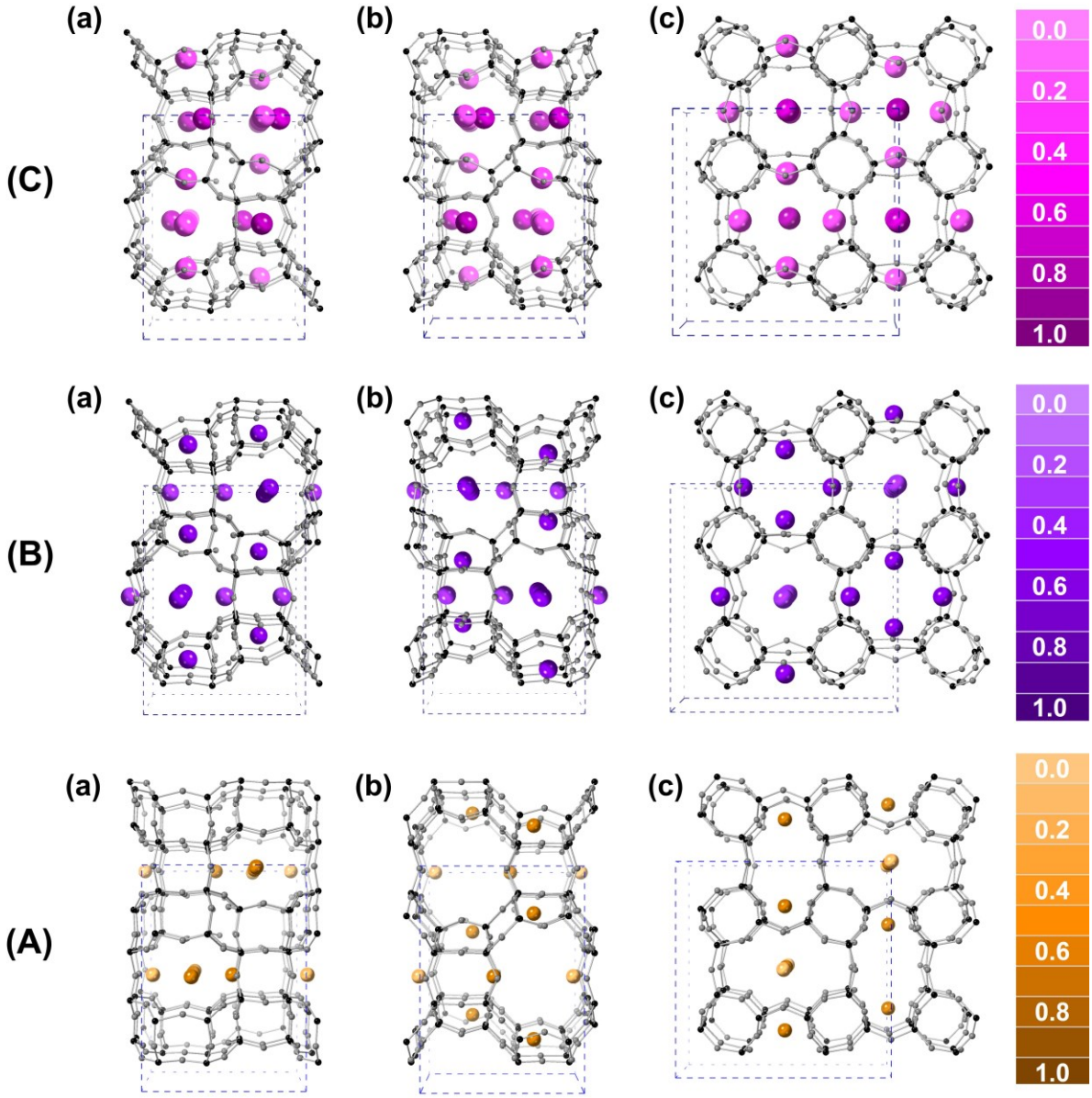

Figure 4. The structures of (A) $Na_{5.0}(K_{1.2})$-, (B) $K_{6.2}$- and (C) $Cs_{6.2}$-MER viewed along (a, b, c) a, b and c axes respectively. Na, K and Cs cations are shown in orange, purple and pink, respectively, with depth of colour reflecting fractional occupancy, as detailed in the legends on the right. T and O sites are shown in black and grey, respectively. Unit cells are indicated by blue dashed lines.

Cook and Conner suggest that due to the thermal motion of zeolite frameworks, the 'free diameters' of windows is effectively 0.7 Å larger than those calculated from the structure in the way described above (the crystallographic free diameters). Therefore, for CO_2, which has kinetic diameter of 3.0 Å, windows with a crystallographic free diameter below 2.3 Å are expected to restrict CO_2 diffusion strongly.[32] As a result, $Na_{6.2}$-MER likely has a 1D channel system for CO_2 in the dehydrated narrow-pore form, as was observed in Li-containing MER

materials,[25] with mean free window diameters *ca*. 2.2 Å wide, based on the trend seen in Figure 5(b). This also agrees with observations in the Si/Al = 3.8 material, which showed that $Na_{6.7}$-MER possessed the narrowest windows of the samples investigated there, as the material optimised Na-O coordination by narrowing windows and shortening Na-O distances. $Na_{6.2}$-MER has the narrowest windows of the materials reported here. They are expected to be larger than its lower silica analogue (the mean free window diameter of $Na_{6.7}$-MER is 2.0 Å) due to the reduced cation content. $K_{6.2}$- and $Cs_{6.2}$-MER also have wider windows than their Si/Al = 3.8 counterparts. Cation occupancies of these materials suggest that Na favours narrow type I and II window sites, shown graphically in Figure S2.6, similar to that seen for the lower Si/Al materials, enabling close Na-O coordination. $K_{6.2}$- and $Cs_{6.2}$-MER have more similar, larger window sizes, with cations requiring longer M-O coordination than Na^+, with most windows slightly larger in the K-form.

A comparison of structural parameters at different Si/Al is shown in Figure 6, with lower silica data obtained from Choi *et al*. and Georgieva *et al*.[23,24] $K_{1.2}Na_{5.0}$-MER is used as a 'Na-form' comparison for the Si/Al = 4.2 material due to the unresolved structure of the pure Na-form. We show later that they possess similar CO_2 adsorption properties.

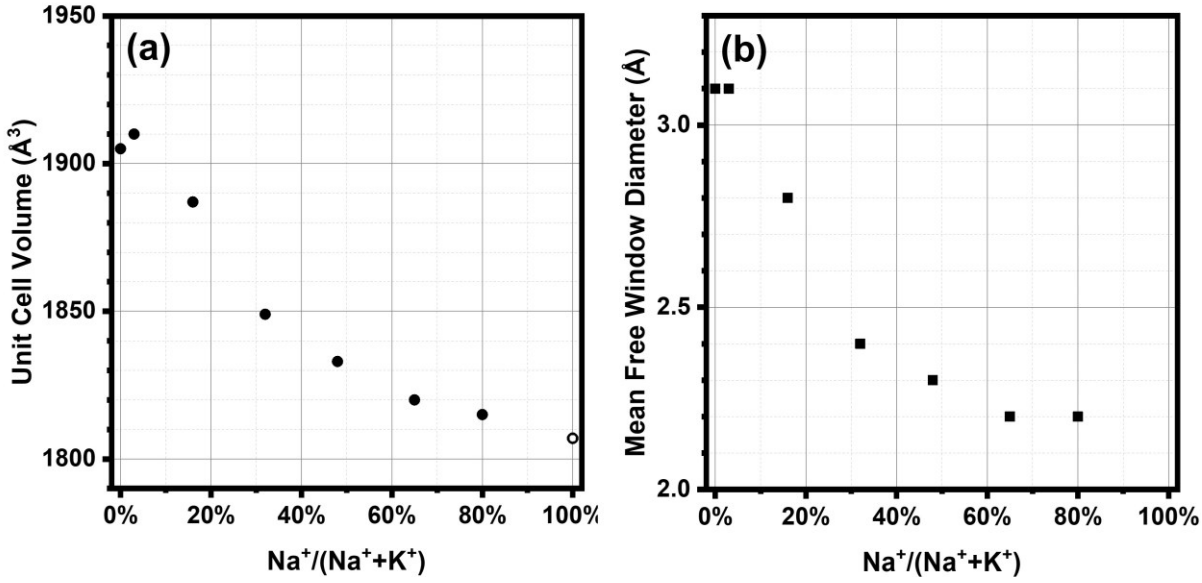

Figure 5. $K_{6.2-x}Na_x$-MER series Rietveld refinement data: (a) unit cell volumes and (b) mean free window diameters with varying Na content. Open circle indicates Immm fit of $Na_{6.2}$-MER.

Figure 6 shows that the smaller cation, Na^+, causes the highest levels of distortion for all materials, with the smallest unit cell volumes and correspondingly narrowest windows. The converse is true for the largest cation, Cs^+ for Si/Al of 2.3 and 3.8, but not for the 4.2 material

reported here. The K-analogue has the largest unit cell volume and most open windows of all forms, because this material no longer occupies a narrow-pore structure upon dehydration. The values of both unit cell volume and mean free window diameter tend to increase as the Si/Al increases and fewer cations occupy the structure. If the window diameter were the sole determinant of diffusivity, Cs-MER samples and $K_{6.2}$-MER would be the fastest adsorbents.

*Table 3. Free diameters of windows, labelled and estimated as described in the text. Those marked by * indicate windows too small to allow passage of CO_2 molecules, also described in text.*

Sample	I	I'	IIa	IIb	III	III'
$Cs_{6.2}$-MER	2.8(1)	2.9(1)	3.0(1)	2.9(1)	2.6(1)	3.0(1)
$K_{6.2}$-MER	3.1(1)	3.2(1)	3.0(1)	2.9(1)	3.4(1)	3.2(1)
$K_{5.7}Na_{0.5}$-MER	3.0(1)	3.3(1)	2.9(1)	3.0(1)	3.3(1)	3.2(1)
$K_{5.2}Na_{1.0}$-MER	2.7(1)	3.1(1)	3.2(1)	2.3(1)	3.0(1)	2.7(1)
$K_{4.2}Na_{2.0}$-MER	2.7(1)	2.3(1)	2.8(1)	2.0(1)	2.5(1)	2.3(1)
$K_{3.2}Na_{3.0}$-MER	2.4(1)	2.3(1)	2.8(1)	1.9(1)	2.2(1)	2.3(1)
$K_{2.2}Na_{4.0}$-MER	2.3(1)	2.0(1)	2.8(1)	1.8(1)	2.2(1)	1.9(1)
$K_{1.2}Na_{5.0}$-MER	2.3(1)	2.0(1)	2.8(1)	1.8(1)	1.9(1)	2.2(1)

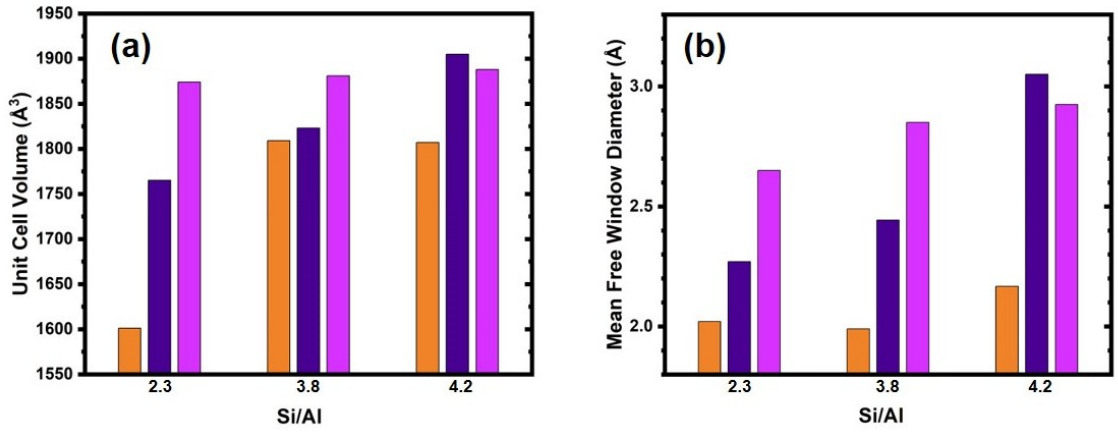

Figure 6. Comparison of (a) unit cell volumes and (b) mean window free diameters for materials with Si/Al = 2.3, 3.8, 4.2. Na-MER, orange; K-MER, blue; Cs-MER, purple. Data for lower silica materials are taken from Choi et al. and Georgieva et al.[23,24] *$K_{1.2}Na_{5.0}$- data is shown in place of $Na_{6.2}$-MER due to unresolved symmetry of the latter.*

Ar adsorption

To measure the degree of "openness" of the materials, the kinetics of Ar adsorption at 303 K were measured with a starting pressure of 800 mbar as described in the experimental, with the data shown in the Figure S3.1. Comparable data was not available for the Si/Al = 2.3 material but a comparison of the relative diffusivities (more precisely the scaled inverse of the diffusional time constant) of the higher Si/Al materials is shown in Figure 7, with the absolute values given in Table 4. As these materials have similar particle sizes (widths *ca.* 300 nm), these will be close to the scaled (relative) diffusivities. SEM images of the two materials are shown in Figures S1.1 and 1.2 for reference. From these it can be seen that values change strongly even over this small change in Si/Al.

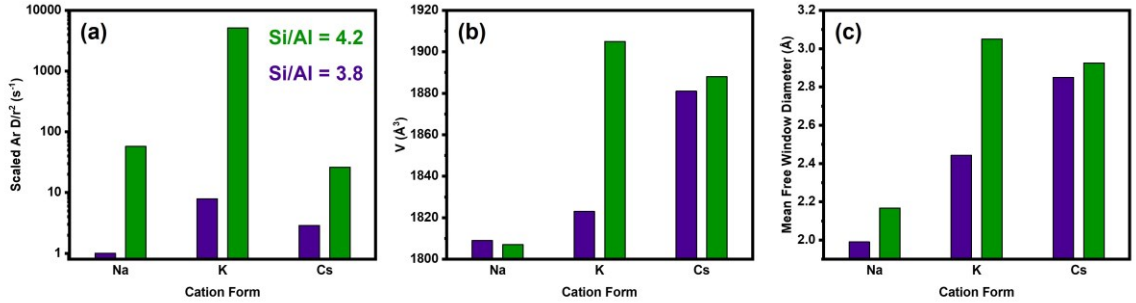

Figure 7. Ar kinetic and structural data of MER: (a) Ar uptake rates at 800 mbar, 303 K, (b) unit cell volumes and (c) mean free window diameters. Data relating to the Si/Al = 3.8 and 4.2 are shown in purple and green, respectively. Diffusivities are scaled relative to the smallest value ($Na_{6.7}$-MER, 8×10^{-5} s^{-1}). $K_{1.2}Na_{5.0}$- window diameter data shown in place of $Na_{6.2}$-MER due to unresolved

Openness is expected to be strongly affected by the window diameters of the framework and blockage of these windows by cations. Comparison of mean free window diameters are shown in Figure 7. In the case of Na-MER materials, window diameters are extremely narrow, however in moving to the higher Si/Al material, the mean free diameter increases by *ca*. 0.2 Å, or 9%, which markedly improves diffusivity. The improvement in Ar diffusivity is not as marked in the case of $Cs_{6.2}$-MER and the increase in window diameter is far less pronounced: for the Cs-form the difference in diffusivity results from fewer cations being close to the limiting *ste* cavities at higher Si/Al. While the number of refined cations in such positions is similar for the two analogues (4.4 and 4.2 total Cs^+ in sites II* and III* for $Cs_{6.7}$- and $Cs_{6.2}$-MER), there are more cations missing from the $Cs_{6.7}$-MER refinement (only 6.0 Cs^+ refined) and so there is likely to be additional blocking from Cs cations not located in the refinement.

While all of the higher Si/Al materials show faster adsorption, the improvement in K-MER is most marked, and $K_{6.2}$-MER allows far more rapid diffusion even than its Si/Al = 4.2 companions, with an improvement of 2 and 3 orders of magnitude over $Cs_{6.2}$-MER (4.2) and the $K_{6.7}$-MER (3.8), respectively. This behaviour is due to the remarkable difference in mean free window diameter, an increase of *ca.* 25% compared to the lower silica material. Although the window diameter is only slightly larger than in the Cs-MER materials, diffusion in $K_{6.2}$-MER is not hindered by such bulky cations occupying vital cavities. This material is not is fast as zeolite 4A, which has an Ar D/r^2 of 48 s^{-1} over ranges of 200-450 K and 0-600 Torr (0-800 mbar).[33] The 2 orders of magnitude difference can again be ascribed to window size differences, with zeolite A possessing a larger free window diameter of any of the materials examined here, over 4 Å.[33,34] An approximation of the uptake timescale can be given by 0.2 r^2/D, as *ca.* 90% of the process has then occurred,[35] and this is also listed in Table 4. A timescale of 0.5 s for $K_{6.2}$-MER highlights the relative rapidity of the higher silica samples.

Table 4. Ar diffusion for MER materials with Si/Al = 3.8 and 4.2.

Cation form	Ar D/r^2 (s^{-1})		Uptake timescale (s)	
	Si/Al = 3.8	**Si/Al = 4.2**	**Si/Al = 3.8**	**Si/Al = 4.2**
Na	8.0×10^{-5}	4.6×10^{-3}	2500	43
K	6.3×10^{-4}	4.1×10^{-1}	317	0.5
Cs	2.3×10^{-4}	2.1×10^{-3}	870	95

Ar adsorption is expected to occur without unit cell expansion due to the noble nature of the gas and hence, as a material which adopts a wide-pore form upon dehydration and without blocking of vital sites by large cations, it is not surprising that $K_{6.2}$-MER exhibits much faster kinetics. After initial adsorption of CO_2, and subsequent transition to a wide-pore form, other materials may possess similar properties.

CO_2 adsorption behaviour

CO_2 sorption isotherms for materials are shown up to 5 bar in Figure 8, at temperatures from 298 to 328 K. Deviations from Type I behaviour (IUPAC nomenclature[36]) are observed in $Na_{6.2}$- and $Cs_{6.2}$-MER as was the case for their lower silica analogues, indicating the same "breathing" behaviour reported there. The kinks associated with this breathing behaviour have

moved to lower pressure for both $Na_{6.2}$- and $Cs_{6.2}$-MER, relative to their MER(3.8) analogues. The steps in adsorption occur at similar CO_2 uptakes for each temperature investigated for a given cation form, indicative of a CO_2-triggered unit cell expansion, but the uptake required to trigger this transition is different for each cation composition.

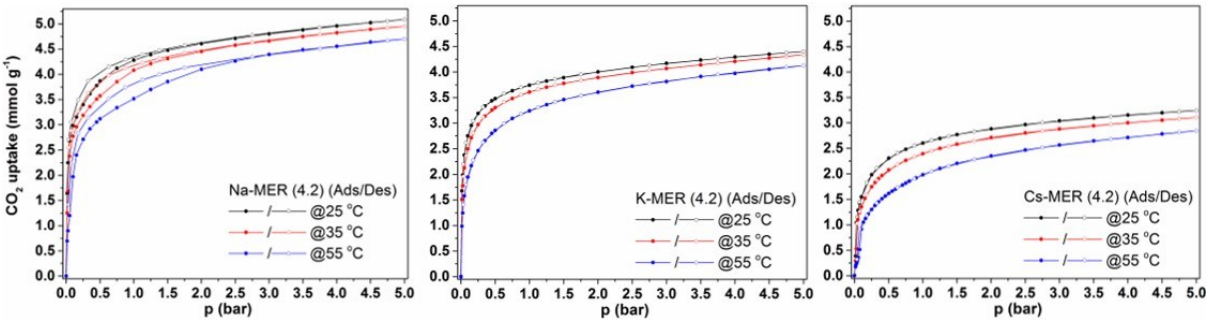

Figure 8. CO_2 sorption isotherms at 298 K for $Na_{6.2}$-, $K_{6.2}$- and $Cs_{6.2}$-MER up to 5 bar. Adsorption and desorption branches are shown in closed and open symbols, respectively.

Uptake at 5 bar and 298 K is increased for all MER (4.2) samples, from 4.3, 3.9 and 2.5 mmol g^{-1} to 4.6, 4.1 and 2.7 mmol g^{-1} for the Na-, K- and Cs-forms of these two Si/Al materials, respectively, which is attributed to increased pore volume upon removal of extra framework cations. The reduced specific uptakes with increasing cation size is expected, with much of this due to normalisation with respect to mass. This particularly affects the $Cs_{6.2}$-MER isotherms, and comparison of molecules per unit cell is shown in Figure S3.3, with more similar uptakes observed for the materials.

Additionally, $Na_{6.2}$-MER shows hysteresis in the desorption branch of its isotherm, suggesting that the sample does not reach equilibrium within the measurement time used in this setup, as was the case for the material we reported earlier.[23] Some, less marked, hysteresis can be seen for $Cs_{6.2}$-MER but not for the $K_{6.2}$-form, suggesting that these materials, especially the latter, have more rapid adsorption and desorption kinetics than the Na-form. The CO_2 adsorption isotherms of the series of Na,K-MER materials (see Figures S3.4 and S4.1) reveal strong hysteresis for $Na_5K_{1.2}$-MER (for which the structure was reported above as being representative of $Na_{6.2}$-MER), but this is reduced for $Na_4K_{2.2}$-MER and absent for $Na_2K_{4.2}$-MER.

The effects of cation type and number on transition pressure are shown in Figure 9. Na-containing materials exhibit inflection points at higher CO_2 pressures than other cation forms, due to the strong energetic preference for contracted windows in the narrow-pore form of the small cations. This was also observed to be the case in Li-containing MER materials with Si/Al

= 4.2, with $Li_{6.2}$-MER adopting a narrow-pore form up to 2.5 bar CO_2 at 298 K.[25] K-analogues always show the lowest pressure inflections, with no phase change observed in the 4.2 material reported here. Increasing Si/Al greatly alters this critical pressure, with a large change observed for Cs-MER materials between Si/Al = 2.3 and 3.8 materials, but also for the smaller change in aluminium content for the higher silica Na-MER materials. Additionally, Choi *et al*. report a $K_{11.8}$-MER (1.7) material which exhibits a kink in adsorption isotherm at *ca*. 0.25 bar,[24] comparable to that of the $Na_{6.2}$-MER (4.2) material, reported here, highlighting the impact of both cation type and number.

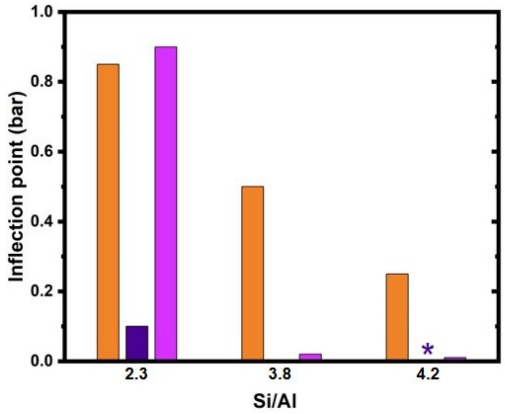

Figure 9. Comparison of inflection points in CO_2 adsorption isotherms at 298 K with varying cation content and Si/Al. Data for lower silica materials are taken from Choi et al. and Georgieva et al.[23,24] *Na-, K- and Cs-materials are indicated by orange, purple and pink bars, respectively. The asterisk at $K_{6.2}$-MER (4.2) indicates that the samples retain a wide-pore form upon dehydration and as such, no inflection point is observed.*

Structural response to CO_2 adsorption

To understand the relationship between structure and CO_2 adsorption, variable pressure XRD (VPXRD) experiments were carried out. Synchrotron data was obtained to allow investigation of the high-pressure regime and enable Rietveld refinement (See Section S5). The experiments gave the series of patterns shown in Figure 10 for pure cation materials. From this it can be seen that, whilst $Na_{6.2}$- and $Cs_{6.2}$-MER undergo a significant change in XRD pattern during adsorption, the K^+-containing material experiences only a mild alteration, corresponding to unit cell expansion. This is in keeping with a $K_{6.2}$-MER material which remains in a wide-pore form upon dehydration, whilst other samples transition from narrow- to wide-pore forms, as observed in Li-containing and the lower silica materials.[23,25]

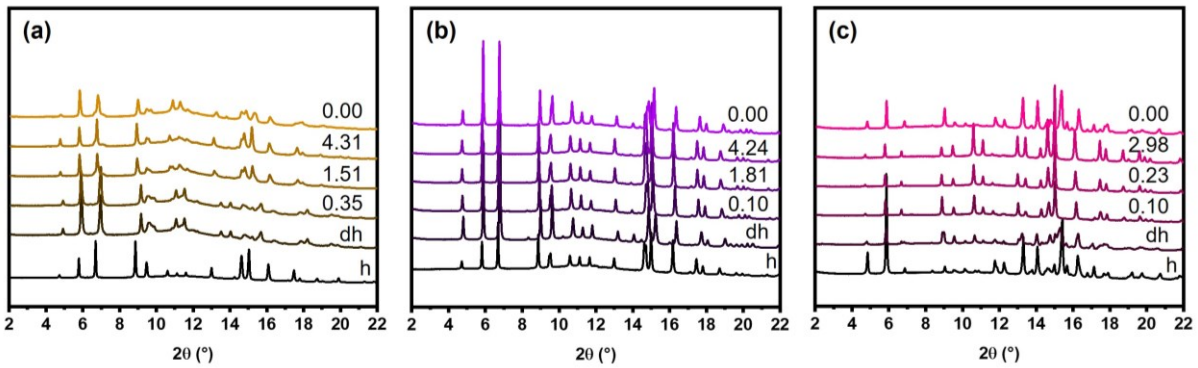

Figure 10. VPXRD patterns for (a) $Na_{6.2}$-, (b) $K_{6.2}$- and (c) $Cs_{6.2}$-MER at 298 K. The pressure of CO_2 during data acquisition is shown in bar on the right of each plot, with hydrated and dehydrated patterns indicated by h and dh, respectively. Patterns denoted 0.00 are those obtained upon desorption.

The $Na_{6.2}$-MER data could not be fitted with the space groups tried, as was the case for the dehydrated sample, but a phase transition clearly occurs after exposure to 1.51 bar of CO_2. The peak shift to lower angle upon CO_2 adsorption is consistent with expansion of the material to adopt a wide-pore structure. Lab-based VPXRD experiments were also carried out to investigate changes in the $Na_{6.2}$-MER pattern from 0 – 1 bar, leaving longer equilibration times between measurements, shown in the Figure 11. A structured fit of these patterns reveals no expansion in unit cell volume below 0.2 bar, followed by a relatively rapid increase from *ca.* 1840 to 1920 $Å^3$. This agrees with the kink observed in the CO_2 adsorption isotherm, suggesting a transition from a narrow- to a wide-pore phase.

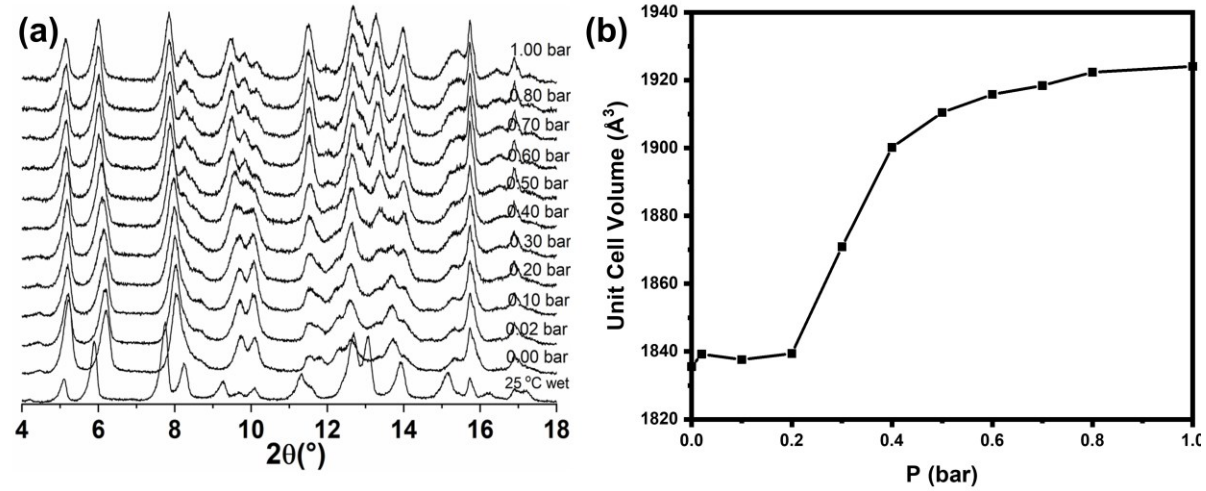

Figure 11. Lab-based in situ VPXRD data for $Na_{6.2}$-MER under a variable pressure of CO_2 at 298 K (a) patterns obtained, with p_{CO2} given on the right and (b) refined unit cell volume as a function of p_{CO2}.

Notably, VPXRD data on the $Na_4K_{2.2}$-MER (4.2) sample that showed no inflection in the CO_2 adsorption isotherm showed unit cell expansion even at 0.02 bar CO_2 at 298 K (see Figure S6.1), indicating that reducing the concentration of the Na^+ cations markedly reduces the tendency for the framework to contract.

$K_{6.2}$-MER does not exhibit such a transition, because it is already in a wide-pore form when dehydrated, but shows some expansion from a unit cell volume of *ca*. 1906 to 1977 $Å^3$, as shown in Figure 12(a). Patterns above 20 mbar are fitted well by the $P4_2/nmc$ space group, as opposed to *Pmmn* observed for the dehydrated material, and CO_2 molecules can be refined within the structure (*ca.* 5.7 molecules of CO_2 per unit cell, shown in Figure 12(b)). The unit cell was found to expand linearly with the refined CO_2 content, as shown in Figure S5.11. The Rietveld plots for the samples with lowest and highest CO_2 content investigated, dehydrated and exposed to 4.24 bar, respectively, are shown in Figure 12(c,d), along with their refined structures. Further details of unit cell volumes and CO_2 content found during refinement are shown in Section S5.2. The lack of a sudden transition from narrow- to wide-pore forms of $K_{6.2}$-MER agrees with its CO_2 sorption isotherms, which show no step, unlike the other samples investigated. Furthermore, cation site occupancies and window geometries barely change upon adsorption, with a mean window free diameter of *ca*. 3.2 Å in all refinements.

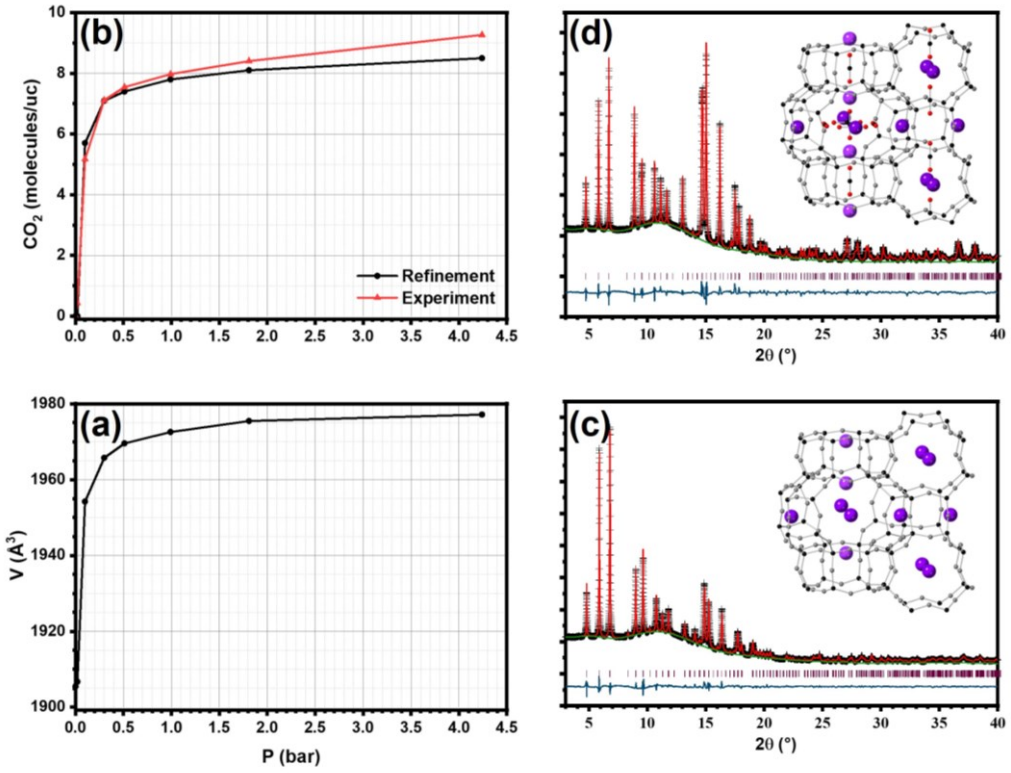

Figure 12. VPXRD refinement data of $K_{6.2}$-MER, including (a) unit cell volume, (b) CO_2 content with pressure and Rietveld plots of $K_{6.2}$-MER under (c) dehydration and (d) 4.24 bar pressure of CO_2, with corresponding refined structures shown inset. Framework T and O sites are shown by black and grey, respectively, K^+ in purple and CO_2 molecules shown in black and red. Plot (b) also contains experimentally expected CO_2 content from adsorption isotherm data.

It is interesting to note that the lower silica analogue, $K_{6.7}$-MER, also exhibits no step in its CO_2 adsorption isotherm: VPXRD experiments showed that whilst the dehydrated form adopted a narrow-pore form, exposure to low pressure CO_2 saw an immediate expansion to a wide-pore form. This was suggested to be due to a fine energetic balance between narrow- and wide-pore forms of $K_{6.7}$-MER. Recent work by Choi *et al*. on MER materials with Si/Al = 1.7 and 2.3 showed a significant step in adsorption of the K-form occurring at *ca*. 0.25 and 0.1 bar, respectively.[24] The high cation content of these materials, (11.9 K^+ for the Si/Al = 1.7 material and 9.7 K^+ for the Si/Al = 2.3 equivalent) would be expected to have greater interactions with the framework and provide an energetic driving force to remain in a narrow-pore form until exposed to a higher pressure of CO_2. A pure silica framework, with no K cations, would remain open in the wide-pore *I*4/*mmm* structure,[34] as there is no driving force for contraction upon dehydration. With only a small change in Si/Al relative to the material we previously reported, we have removed sufficient cations for the wide-pore form to remain the most energetically favourable structure upon desorption at 298 K and above. Whilst increasing Si/Al further may

have impacts on adsorption properties of K-MER, with window occupancies decreasing, it is unlikely to have as great an effect as achieved in moving from Si/Al = 3.8 to 4.2.

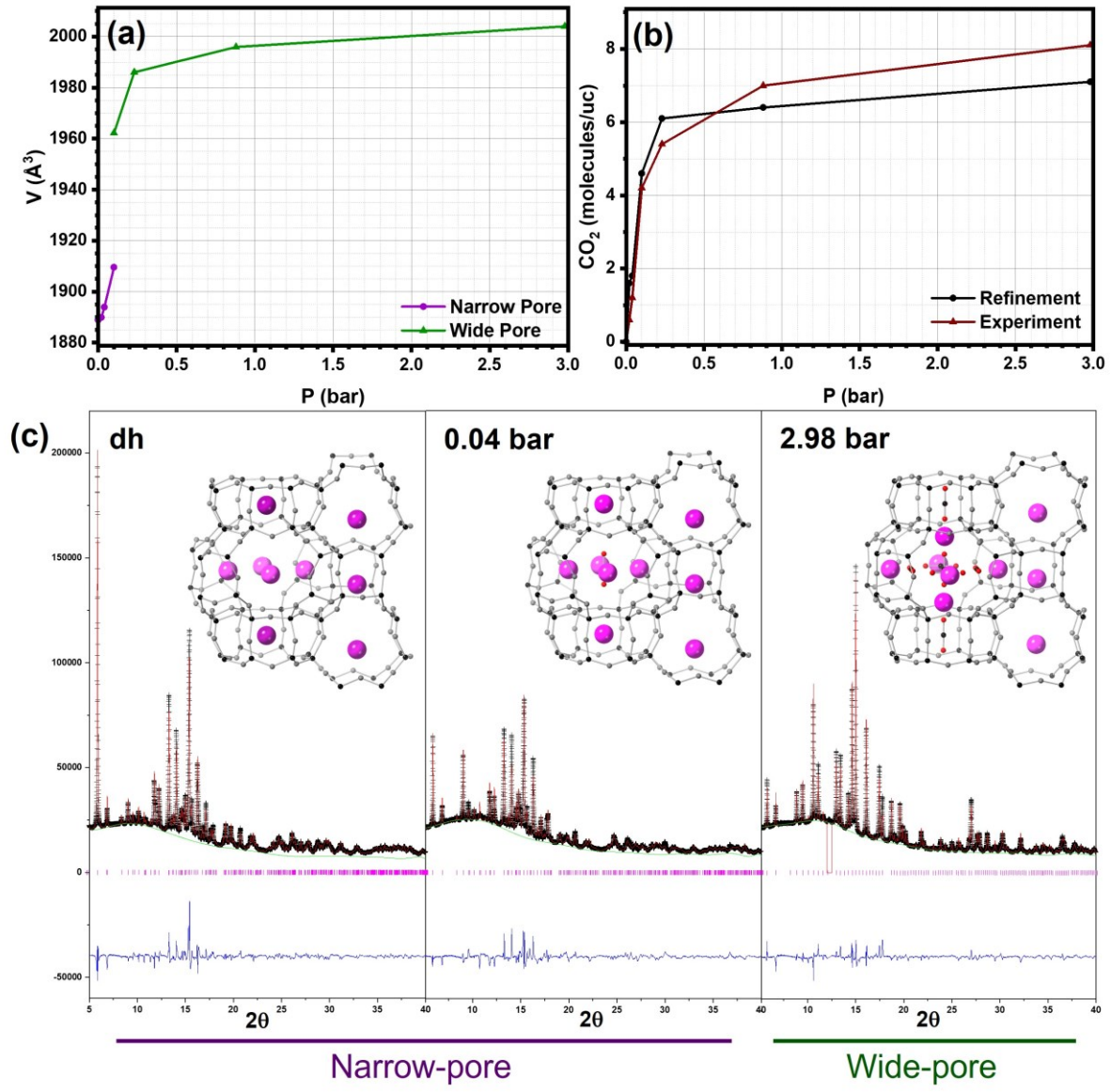

Figure 13. VP Synchrotron XRD refinement data of $Cs_{6.2}$-MER, including (a) unit cell volume, (b) CO_2 content with pressure and (c) Rietveld plots of $K_{6.2}$-MER under dehydration, 0.04 bar and 2.98 bar pressure of CO_2, with corresponding refined structures shown beneath. Framework T and O sites are shown by black and grey, respectively, Cs^+ in pink and CO_2 molecules shown in black and red. Plot (b) also contains experimentally expected CO_2 content from adsorption isotherm data.

$Cs_{6.2}$-MER exhibits a phase transition during VPXRD experiments, as was the case for $Na_{6.2}$-MER, corresponding to a transition between different pore forms. Refinement details for this material are shown in Figure 13, including unit cell volume and refined CO_2 content as well as fits and structures for selected pressures. Two phases are observed together at 0.1 bar, with unit cell volumes of 1911 and 1965 Å^3, respectively. This may be an indication of the relative

favourability of the two phases at this CO_2 potential, slow kinetics of transition or possibly related to limitations of the experimental setup. Below and above this point, only narrow- or wide-pore forms are observed, which is consistent with the kink observed in the CO_2 adsorption isotherm of the material. As is the case for $K_{6.2}$-MER, the dehydrated $Cs_{6.2}$-MER adopts the *Pmmn* space group, but upon exposure of the material to CO_2, $P4_2/nmc$ is a suitable description. Full refinement data is given in Section S5.1.

*Table 5. Cation site distribution in $Cs_{6.2}$-MER with varying p_{CO2} determined by Rietveld refinement. Site labelling is as described in the text, with sites denoted by * indicating merging of related sites i.e. III, III'. For each sample the multiplicity (M), fractional occupancy and number of cations per unit cell are given.*

Condition	Ia			IIa			III*		
	M	frac. occ	atoms/uc	M	frac. occ	atoms/uc	M	frac. occ	atoms/uc
dh	2	0.80(1)	1.6(1)	4	0.37(1)	1.5(1)	4	0.69(1)	2.8(1)
0.04 bar	2	0.47(1)	0.9(1)	8	0.29(1)	2.3(1)	4	0.59(1)	2.4(1)

Condition	I			II			III		
	M	frac. occ	atoms/uc	M	frac. occ	atoms/uc	M	frac. occ	atoms/uc
2.98 bar	4	0.46(1)	1.8(1)	8	0.35(1)	2.8(1)	4	0.29(1)	1.2(1)

Measurement of the PXRD pattern *via* synchrotron PXRD conducted with high p_{CO2} resolution allows greater insight into the mechanism by which Cs-MER materials change between narrow- and wide-pore forms than was achieved for the Si/Al = 3.8 material.[23] A summary of cation locations with varying pressure is given in Table 5, with a more detailed description in the section S5.1. In the low-pressure (narrow-pore) regime upon exposure to CO_2, some Cs cations move from the centre of the *d8r* unit (site Ia) to site IIa, which is driven by favourable interactions between Cs^+ and the adsorbate. Upon transition to the higher-pressure regime, Cs cations again relocate, with sites I and II preferred and no cations in site Ia. The relocation to site I is associated with CO_2 molecules occupying the *d8r* unit. The occupancy of site I is too high to arise solely from cations previously in site Ia and a decrease in site III occupancy is observed. This suggests Cs cations hop from site II to I and from site III to II, which may be a concerted mechanism, as shown in Figure 14. CO_2 within the *d8r* unit may improve the

energetics of site I, providing a thermodynamic drive for cation relocation, and CO_2 movement may aid cation relocation. The overall behaviour is similar to that observed in the Si/Al = 3.8 material, with Cs^+ initially favouring site Ia and relocating to sites I and II at high uptake of CO_2. (The same intermediate site migration may occur in the lower silica material but VPXRD data was not collected in the relevant low pressure region.) Window geometries also change, with the mean free diameter of windows increasing from 2.9 to 3.5 Å in the narrow- and wide-pore forms adopted at low and high pressure, respectively.

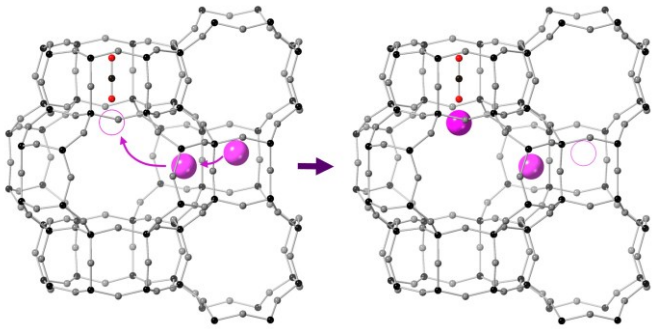

Figure 14. Schematic representation of a postulated Cs^+ migration mechanism. Cs cations initially in sites II and III move to occupy sites I and II. CO_2 sited in the d8r unit may provide thermodynamic driving force for this migration or may accelerate it. Framework T and O sites are shown in black and grey, respectively; Cs^+ in pink and CO_2 molecules in black and red.

Kinetics of CO_2 adsorption and desorption

To measure the CO_2 diffusivity in the Na-, K- and Cs-MER (4.2) materials and so understand the kinetics of their adsorption and desorption, zero-length column (ZLC) experiments were performed on all three materials (see Section S7 for details). The measured diffusivities at low CO_2 loadings could then be compared with values obtained *via* similar analyses on their Si/Al = 3.8 analogues.[23]

These ZLC experiments follow the concentration of CO_2 in the effluent gas obtained using a He carrier gas flow during desorption, following adsorbent equilibration in a 10% CO_2 flow in He at 298 K. For Na- and Cs-MER, the adsorbate and gas flow are initially in equilibrium during desorption, indicating that diffusion is too rapid to be quantified by this method when the materials are in the wide-pore phase. However, at longer desorption times and therefore at low adsorbate concentrations, when the structures are in the narrow-pore phase, it is possible to determine the diffusivities. Both Na- and Cs-MER materials in the narrow-pore form showed improved kinetics at 298 K, relative to their Si/Al = 3.8 analogues, with D/r^2 values increasing

from 2.2×10^{-4} to 8.6×10^{-4} s^{-1} and 9.0×10^{-4} to 6.9×10^{-3} s^{-1}, respectively, as the cation content decreased. Also, because $Na_{6.2}$- and $Cs_{6.2}$-MER undergo the narrow-to-wide pore phase transitions at lower partial pressure than that observed in their higher silica analogues, kinetic limitations will disappear at relatively low CO_2 pressures during adsorption and diffusivity become more rapid as the materials move from kinetic to equilibrium-controlled adsorption behaviour upon expansion to their wide-pore forms.

The diffusivity of CO_2 in $K_{6.2}$-MER was too fast to be measured using this technique, showing equilibrium-controlled desorption throughout the entire experiment. This is because $K_{6.2}$-MER adopts a wide-pore form even when empty and its 8R windows remain relatively wide, as shown in Table 3. Notably in $K_{6.7}$-MER at very low loadings, where the narrow-pore form is stable, D/r^2 was lower, and determined to be 2.5×10^{-4} s^{-1} at 298 K.

Whilst Choi *et al*. did not report diffusivity values, it can be seen from their kinetic work that the same trend in diffusivity is seen in their Si/Al = 2.3 material, with the Na-form showing the slowest kinetics followed by the $Cs_{9.7}$-MER (2.3) material, and $K_{9.7}$-MER (2.3) showing the most rapid uptake of CO_2.[24]

These ZLC results show rapid sorption behaviour for both $K_{6.7}$- and $K_{6.2}$-MER but do not allow comparison of these materials in the wide-pore form. Qualitative sorption studies were therefore carried out, as described in the experimental section. By exposing samples to CO_2 and monitoring the pressure drop over time, this allows us to compare the relative rates of adsorption, although heating effects prohibit extrapolation of kinetic parameters. These results are shown in Figure 15, with the pressure drop far more rapid for the Si/Al = 4.2 material, and correspondingly faster CO_2 uptake. This indicates that, whilst the kinetics of both materials are extremely rapid on a ZLC timescale, the new $K_{6.2}$-MER material exhibits faster uptake.

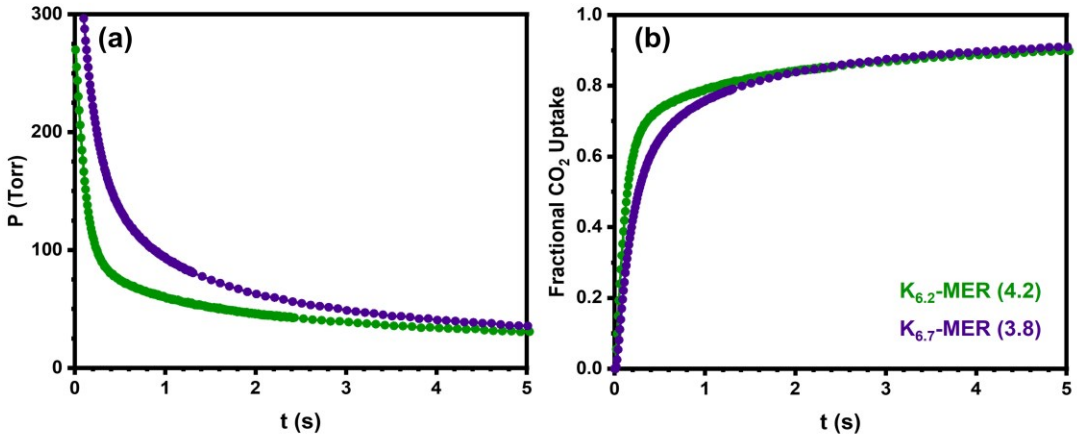

Figure 15. Qualitative CO_2 kinetic data for K-MER materials at 303 K: (a) CO_2 pressure over time and (b) CO_2 uptake over time, as a fraction of uptake after 500 s. Si/Al = 3.8 and 4.2 data are shown in purple and green, respectively.

Examination of cation sites and window sizes (detailed in Table 2 and Table 3) within the materials help to give a structural explanation for the kinetic behaviour observed in these materials. $Na_{6.2}$-MER has the narrowest windows, and its relatively poor kinetics can be attributed to the hindrance of molecular diffusion by narrow window sizes, although cation siting may also play a role. Discrepancies between $K_{6.2}$- and $Cs_{6.2}$-MER cannot be ascribed to window dimensions as they possess similar window sizes, as discussed earlier. Instead, differences between the 2 materials lie in cation siting. In the Cs-material both sets of *ste* cavities show high occupancy by large Cs cations, as well as the *d8r* unit and hence, whilst window sizes are large enough for rapid diffusion of CO_2, transmission along all channels within the material are obstructed by Cs^+. For percolation through the material to occur, cation motion is required as described by the cation gating mechanism,[37] and hence diffusivity suffers. As there are fewer cations in this material than in the Si/Al = 3.8 material, and window sizes in channels along *a* and *b* are larger, diffusivity is improved. Choi *et al*. suggest a cooperative cation-gating – breathing mechanism in their low silica material,[24] while we consider these effects are separate in the higher silica materials, cation-gating being a kinetic phenomenon whilst breathing depends on thermodynamic factors. $K_{6.2}$-MER contains K cations, which would be expected to be more mobile than Cs^+, and as cations occupy sites II*, as opposed to sites III*, they would more readily move out of the path of CO_2 molecules percolating through the structure, with poorer coordination to the anionic framework.

While the fast kinetic behaviour of $K_{6.2}$-MER is encouraging, it is by no means the only property required for application in carbon capture technologies, such as natural gas and biogas upgrading. As discussed, the high degree of "openness" of the material might be expected to have a negative impact on CO_2/CH_4 selectivity. To this end, further kinetic testing was carried out in the form of breakthrough experiments. Gas streams were composed of 10% CO_2/40% CH_4 in He and experiments were carried out at 308 K. The resulting breakthrough sorption curves are shown in Figure 16, plotted against eluted volume *per* mmol of sample (Ft/N) to allow more ready comparison of materials with significant differences in molar mass. In $Na_{6.2}$- and most notably $Cs_{6.2}$-MER, steps are observed in the breakthrough curves, consistent with phase transitions from narrow- to wide-pore structures. As there is no such transition in the $K_{6.2}$-MER material, there is no kink in the breakthrough curve, allowing for a pure stream of CH_4 for a longer period.

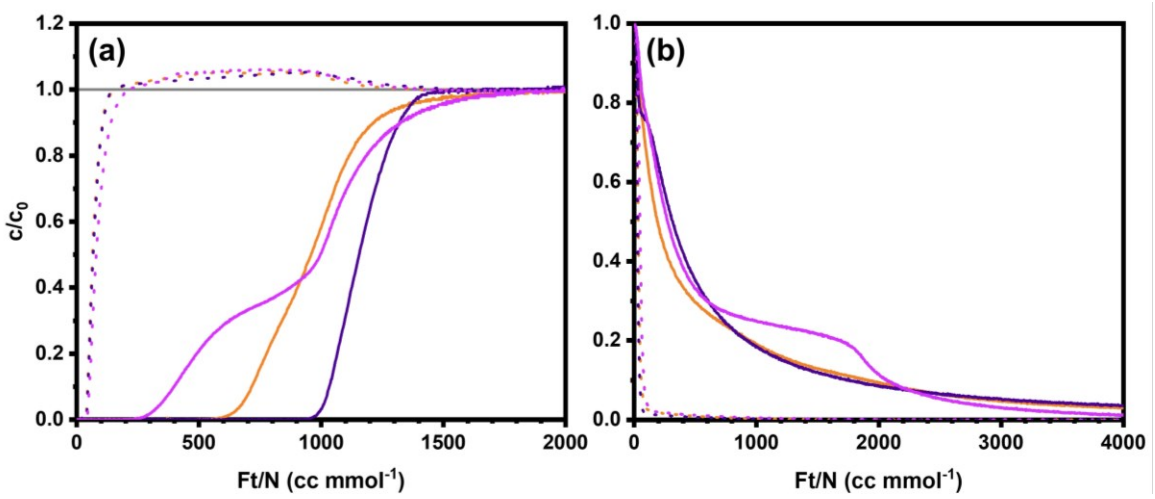

Figure 16. Breakthrough (a) adsorption and (b) desorption curves for MER (4.2) materials at 308 K. CO_2 and CH_4 data is indicated by solid and dotted lines, with $Na_{6.2}$-, $K_{6.2}$- and $Cs_{6.2}$-MER sample data shown in orange, purple and pink, respectively.

CO_2/CH_4 selectivity values are given in

Table 6. The more open $K_{6.2}$-MER material possesses lower adsorption selectivity compared to the other materials. The Na-form retains the same selectivity as the Si/Al = 3.8 analogue, whilst the Cs-form of MER (4.2) shows very high selectivity, as was the case for $K_{6.7}$-MER (3.8).

Table 6. CO_2/CH_4 selectivities of MER materials as determined by breakthrough experiments. Si/Al = 3.8 and 4.2 data were collected at 298 and 308 K, respectively. Breakthrough curves for the two materials are compared in Figure S8.1.

Cation form	CO_2/CH_4 selectivity	
	Si/Al = 3.8	Si/Al = 4.2
Na	303	282
K	850	154
Cs	340	808

The two K-MER samples are shown to have very rapid CO_2 kinetics from ZLC experiments, and, based on these selectivity values, $K_{6.7}$-MER (3.8) would appear to be the better sorbent. The improved kinetics of $K_{6.2}$-MER (4.2), and the smaller change in volume upon adsorption (6% and 3% expansion in volume upon exposure to 0.5 bar CO_2 for $K_{6.7}$-MER (3.8) and $K_{6.2}$-MER (4.2), respectively)[23], may, however, provide advantages for application, such as enabling a faster flow rate to be used during kinetic separations. This material was therefore examined in more detail, via estimation of the heat of CO_2 adsorption and the properties of a pelletised sample with alumina.

Isosteric heats of CO_2 adsorption between *ca*. 40 and 32.5 kJ mol^{-1} (at 2 and 3.5 mmol g^{-1}, respectively, were measured from the isotherms via the Clausius-Clapeyron method as described in Section S9. Values. Accurate isotherm data was not available at the lower pressures at which lower uptakes were achieved. An independent estimate of 35 ± 1 kJ mol^{-1} for the the Henry law region was made via the ZLC data, also described in Section S9. These values are consistent with other heats of adsorption of CO_2 measured for K-forms of the zeolites Y (34 - 39 kJ mol^{-1})[38] and L (35 kJ mol^{-1}).[39]

As the $K_{6.2}$-MER material shows rapid kinetics, reasonable CO_2/CH_4 selectivity, and furthermore was available in >20 g batches, we investigated it for application by embedding the powder within alumina beads, as described in the experimental section. No crystallisation of alumina hydrate was observed upon heating the mixture at 573 K for 12 h, as shown by XRD in Figure S10.1. The resulting breakthrough curves on beads of different sizes, measured under identical conditions, are shown in Figure 17, plotted *vs* eluted volume with respect to mass of

$K_{6.2}$-MER, along with images of the beads. The uptakes of the pelletised samples, normalised on zeolite mass, are consistent with the binder content of ca. 35 wt%.

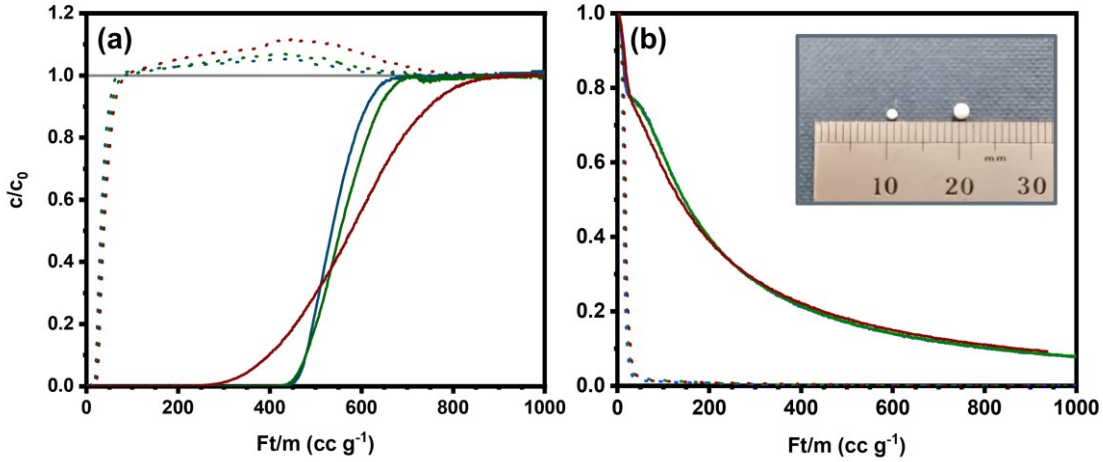

Figure 17. Breakthrough (a) adsorption and (b) desorption curves for forms of $K_{6.2}$-MER at 308 K. CO_2 and CH_4 data is indicated by solid and dotted lines, with powder, 1 mm and 2 mm bead sample data shown in blue, green and red, respectively. Images of the beads are shown inset. Note that desorption curves of powder and 1 mm beads overlap.

Although the use of 2 mm beads introduces some macropore diffusion limitations, consistent with fast diffusion in the micropores, incorporation into the smaller 1 mm beads has a negligible effect on the zeolite's performance and gives the same kinetic behaviour as the powder, with the advantage of being more appropriate for industrial application.

Ultimately the choice of bead size would depend on the process configuration of choice and would take into account the pressure drop and mass transfer limitations consistent with small and large beads, respectively. Here we have shown the potential for the pelletisation of this material, consistent with application for CO_2 separation from CH_4.

Conclusions

The Na, K and Cs forms of a high silica merlinoite (Si/Al = 4.2) have been prepared and their adsorption properties measured for Ar and CO_2. These have been related to their crystal structures determined both in the dehydrated form and during CO_2 uptake by *in situ* PXRD at laboratory and synchrotron sources.

The framework of merlinoite is flexible, and its response to dehydration is strongly dependent on the type of alkali metal cation present because of their different cationic radii and charge densities. $Na_{6.2}$-MER (4.2) shows strong unit cell contraction and a framework with narrow pores due to structural distortion to give closer Na-O coordination. It has not yet been possible to establish the structure of the pure Na end member, but some details can be extrapolated from the structure determination of members of a $K_{6.2-x}Na_x$-MER series extending to *x* values as high as 5.0: furthermore, $Na_5K_{1.2}$-MER performs similarly to $Na_{6.2}$-MER as a CO_2 adsorbent. By contrast, $K_{6.2}$-MER (4.2) shows little framework contraction and remains in a wide-pore form because of the weaker cation-framework interactions. In $Cs_{6.2}$-MER (4.2), the larger cations display a very different cation site distribution and the narrow-pore dehydrated form is much less strongly contracted compared to its wide-pore form than it is for $Na_{6.2}$-MER (4.2). This cation-dependent MER behaviour is similar to that observed for $Na_{6.7}$-MER (3.8) and $Cs_{6.7}$-MER (3.8), but not for $K_{6.7}$-MER (3.8), where a narrow-pore structure is observed during dehydration. This demonstrates that the energies of narrow- and wide-pore forms of K-MER (and the competition between the energetic cost of distortion versus the benefit of closer cation coordination) are finely balanced for K-MER in this compositional range.

Ar uptake kinetics in MER (4.2) at 303 K reflect the influence of the window sizes and cation occupancies of these dehydrated forms, and the diffusivities increase in the order Na < Cs << K. The slow uptake in $Na_{6.2}$-MER (4.2) and to a lesser extent $Cs_{6.2}$-MER (4.2) reflects the narrow windows, while the more open $K_{6.2}$-MER (4.2) allows very rapid uptake. In all cases the uptake is, remarkably, much faster in the MER (4.2) than in the MER (3.8) samples. This must arise from faster percolation through more empty windows in Na- and Cs-MER materials since the unit cells are similar sizes for both framework compositions. The *ca*. 3 orders of magnitude increase going from $K_{6.7}$-MER (3.8) to $K_{6.2}$-MER (4.2) results from both an increase in window size and a reduction in blocking cations.

Measurement of CO_2 adsorption isotherms and associated *in situ* PXRD enable the behaviour of these structures in response to CO_2 adsorption to be related to changes in unit cell volume

and framework conformation, and for the K- and Cs-forms this can be related to measured cation site locations. Both Na- and Cs-forms exhibit a phase change from narrow to wide pore which leads to stepped isotherms. It is possible in $Cs_{6.2}$-MER (4.2) to identify the change in Cs cation site location associated with this *via* high resolution synchrotron diffraction, where Cs cations move into sites that have better access to adsorbed CO_2 molecules and the framework consequently relaxes. By contrast, $K_{6.2}$-MER (4.2) starts in a wide-pore form and expands gradually as adsorption proceeds. Comparison with merlinoites with lower Si/Al ratios shows that reducing the cation content reduces the pressure at which the narrow-to-wide pore transition occurs, because there is less coulombic interaction keeping the framework closed to overcome by solvating the cations.

The kinetics of CO_2 adsorption, as measured by zero length column, CO_2 uptake and breakthrough curve shape, indicate that $K_{6.2}$-MER (4.2) has the most suitable characteristics (the highest diffusivity) to achieve pure methane from mixed CO_2/CH_4 gas streams, although the equilibrium CO_2 selectivity from the gas mixture is lower than for the other cation forms. With methane production in mind, it was possible to prepare $K_{6.2}$-MER (4.2) in pelletised form using alumina binder, and 1 mm beads were found to retain the excellent performance of the $K_{6.2}$-MER (4.2) powder in breakthrough tests, of potential significance for application.

These studies underline the great structural complexity that results from the variation of framework composition and cation content of flexible zeolites such as merlinoite, and the consequent variation in adsorption properties for both inert gases such as Ar and adsorbates such as CO_2 that interact strongly with the charge-balancing cations. One advantage of this adaptability may be the possibility to tune the performance of these adsorbents to a very high degree for target gas separations, if their structural chemistry is understood.

Supporting Information

Supporting Information is available free of charge on the ACS Publications website at [doi**********] including: scanning electron microscopy; powder X-ray diffraction and crystallographic analysis (including cif files) on hydrated, dehydrated and CO_2-loaded merlinoites; kinetic Ar and CO_2 uptake curves, experimental CO_2 adsorption isotherms and variable temperature ZLC data and its kinetic analysis.

Acknowledgements

The authors thank the EPSRC for funding (Cation-controlled gating for selective gas adsorption over adaptable zeolites: EP/N032942/1, V.M.G., P.A.W.; EP/N033329/1, M.C.V. and S.B.; an NPIF Ph.D. scholarship for E.L.B.: EP/R512199/1). We acknowledge Diamond Light Source for beamtime on Beamline I11 under Proposal CY22322-1. Dr. Yuri Andreev (University of St. Andrews) is thanked for assistance with *in situ* PXRD measurements. The research data supporting this publication can be accessed at https://doi.org/10.17630/2adf2961-a318-41f1-ad3a-ad3d49ad210e

References

(1) Vanelderen, P.; Vancauwenbergh, J.; Sels, B. F.; Schoonheydt, R. A. Coordination Chemistry and Reactivity of Copper in Zeolites. *Coord. Chem. Rev.* **2013**, *257*, 483–494.

(2) Dabrowski, A.; Hubicki, Z.; Podkocielny, P.; Robens, E. Selective Removal of the Heavy Metal Ions from Waters and Industrial Wastewaters by Ion-Exchange Method. *Chemosphere* **2004**, *56*, 91–106.

(3) Gaffney, T. R. Porous Solids for Air Separation. *Curr. Opin. Solid State Mater. Sci.* **1996**, *1*, 69–75.

(4) Gao, W.; Liang, S.; Wang, R.; Jiang, Q.; Zhang, Y.; Zheng, Q.; Xie, B.; Toe, C. Y.; Zhu, X.; Wang, J. *et al*. Industrial Carbon Dioxide Capture and Utilization: State of the Art and Future Challenges. *Chem. Soc. Rev.* **2020**, *49*, 8584–8686.

(5) Buonomenna, M. G. Membrane Processes for a Sustainable Industrial Growth. *RSC Adv.* **2013**, *3*, 5694–5740.

(6) Sai Bhargava Reddy, M.; Ponnamma, D.; Sadasivuni, K. K.; Kumar, B.; Abdullah, A. M. Carbon Dioxide Adsorption Based on Porous Materials. *RSC Adv.* **2021**, *11*, 12658–12681.

(7) Villadsen, S. N. B.; Fosbøl, P. L.; Angelidaki, I.; Woodley, J. M.; Nielsen, L. P.; Møller, P. The Potential of Biogas; the Solution to Energy Storage. *ChemSusChem* **2019**, *12*, 2147–2153.

(8) IEA. *Carbon Capture and Storage : The Solution for Deep Emissions Reductions*; 2015.

(9) Cavenati, S.; Grande, C. A.; Rodrigues, A. E.; Kiener, C.; Müller, U. Metal Organic Framework Adsorbent for Biogas Upgrading. *Ind. Eng. Chem. Res.* **2008**, *47*, 6333–6335.

(10) Chen, X. Y.; Vinh-Thang, H.; Ramirez, A. A.; Rodrigue, D.; Kaliaguine, S. Membrane Gas Separation Technologies for Biogas Upgrading. *RSC Adv.* **2015**, *5*, 24399–24448.

(11) Cheung, O.; Hedin, N. Zeolites and Related Sorbents with Narrow Pores for CO_2 Separation from Flue Gas. *RSC Adv.* **2014**, *4*, 14480–14494.

(12) Remy, T.; Gobechiya, E.; Danaci, D.; Peter, S. A.; Xiao, P.; Van Tendeloo, L.; Couck, S.; Shang, J.; Kirschhock, C. E. A.; Singh, R. K. *et al*. Biogas Upgrading through Kinetic Separation of Carbon Dioxide and Methane over Rb- and Cs-ZK-5 Zeolites. *RSC Adv.* **2014**, *4*, 62511–62524.

(13) Ghosh, S.; Modak, A.; Samanta, A.; Kole, K.; Jana, S. Recent Progresses in Materials Development for CO_2 Conversion: Issues and Challenges. *Mater. Adv.* **2021**, 2, 3161-3187.

(14) Liu, Q.; Mace, A.; Bacsik, Z.; Sun, J.; Laaksonen, A.; Hedin, N. NaKA Sorbents with High CO_2-over-N_2 Selectivity and High Capacity to Adsorb CO_2. *Chem. Commun.* **2010**, *46*, 4502–4504.

(15) Shang, J.; Hanif, A.; Li, G.; Xiao, G.; Liu, J. Z.; Xiao, P.; Webley, P. A. Separation of CO_2 and CH_4 by Pressure Swing Adsorption Using a Molecular Trapdoor Chabazite Adsorbent for Natural Gas Purification. *Ind. Eng. Chem. Res.* **2020**, *59*, 7857–7865.

(16) Palomino, M.; Corma, A.; Jordà, J. L.; Rey, F.; Valencia, S. Zeolite Rho: A Highly Selective Adsorbent for CO_2/CH_4 Separation Induced by a Structural Phase Modification. *Chem. Commun.* **2012**, *48*, 215–217.

(17) Lozinska, M. M.; Mangano, E.; Mowat, J. P. S.; Shepherd, A. M.; Howe, R. F.; Thompson, S. P.; Parker, J. E.; Brandani, S.; Wright, P. A. Understanding Carbon Dioxide Adsorption on Univalent Cation Forms of the Flexible Zeolite Rho at Conditions Relevant to Carbon Capture from Flue Gases. *J. Am. Chem. Soc.* **2012**, *134*, 17628–17642.

(18) Lozinska, M. M.; Mowat, J. P. S.; Wright, P. A.; Thompson, S. P.; Jorda, J. L.; Palomino,

M.; Valencia, S.; Rey, F. Cation Gating and Relocation during the Highly Selective "Trapdoor" Adsorption of CO_2 on Univalent Cation Forms of Zeolite Rho. *Chem. Mater.* **2014**, *26*, 2052–2061.

(19) Lozinska, M. M.; Mangano, E.; Greenaway, A. G.; Fletcher, R.; Thompson, S. P.; Murray, C. A.; Brandani, S.; Wright, P. A. Cation Control of Molecular Sieving by Flexible Li-Containing Zeolite Rho. *J. Phys. Chem. C* **2016**, *120*, 19652–19662.

(20) Cheung, O.; Wardecki, D.; Bacsik, Z.; Vasiliev, P.; McCusker, L. B.; Hedin, N. Highly Selective Uptake of Carbon Dioxide on the Zeolite $|Na_{10.2}KCs_{0.8}|$-LTA - a Possible Sorbent for Biogas Upgrading. *Phys. Chem. Chem. Phys.* **2016**, *18*, 16080–16083.

(21) Rzepka, P.; Wardecki, D.; Smeets, S.; Müller, M.; Gies, H.; Zou, X.; Hedin, N. CO_2-Induced Displacement of Na^+ and K^+ in Zeolite |NaK|-A. *J. Phys. Chem. C* **2018**, *122*, 17211–17220.

(22) Du, T.; Fang, X.; Liu, L.; Shang, J.; Zhang, B.; Wei, Y.; Gong, H.; Rahman, S.; May, E. F.; Webley, P. A. *et al*. An Optimal Trapdoor Zeolite for Exclusive Admission of CO_2 at Industrial Carbon Capture Operating Temperatures. *Chem. Commun.* **2018**, *54*, 3134–3137.

(23) Georgieva, V. M.; Bruce, E. L.; Verbraeken, M. C.; Scott, A. R.; Casteel, Jr, W. J.; Brandani, S.; Wright, P. A. Triggered Gate Opening and Breathing Effects during Selective CO_2 Adsorption by Merlinoite Zeolite. *J. Am. Chem. Soc.* **2019**, *141*, 12744–12759.

(24) Choi, H. J.; Jo, D.; Min, J. G.; Hong, S. B. The Origin of Selective Adsorption of CO_2 on Merlinoite Zeolites. *Angew. Chemie - Int. Ed.* **2020**, *60*, 4307–4314.

(25) Georgieva, V. M.; Bruce, E. L.; Chitac, R. G.; Lozinska, M. M.; Hall, A. M.; Murray, C. A.; Smith, R. I.; Turrina, A.; Wright, P. A. Cation Control of Cooperative CO_2 Adsorption in Li-Containing Mixed Cation Forms of the Flexible Merlinoite Zeolite. *Chem. Mater.* **2021**, *33*, 1157–1173.

(26) Brandani, S.; Ruthven, D. M. Analysis of ZLC Desorption Curves for Gaseous Systems. *Adsorption* **1996**, *2*, 133–143.

(27) Ruthven, D. M.; Kärger, J.; Brandani, S.; Mangano, E. Sorption Kinetics: Measurement of Surface Resistance. *Adsorption* **2021**, *27*, 787–799.

(28) Hu, X.; Brandani, S.; Benin, A. I.; Willis, R. R. Development of a Semi-automated Zero Length Column Technique for Carbon Capture Applications: Rapid Capacity Ranking of Novel Adsorbents. *Ind. Eng. Chem. Res.* **2015**, *54*, 6772–6780.

(29) Brandani, S.; Mangano, E. The Zero Length Column Technique to Measure Adsorption Equilibrium and Kinetics: Lessons Learnt from 30 Years of Experience. *Adsorption* **2021**, *27*, 319–351.

(30) Verbraeken, M. C.; Centineo, A.; Canobbio, L.; Brandani, S. Accurate Blank Corrections for Zero Length Column Experiments. *Adsorption* **2021,** 27, 129–145.

(31) Coelho, A. *TOPAS-Academic*; Coelho Software: Brisbane, Australia, 2016.

(32) Cook, M.; Conner, W. C. How Big Are the Pores of Zeolites? In *Proceedings of the 12th International Zeolite Conference*; Treacy, M. M. J., Marcus, B. K., Bisher, M. E., Higgins, J. B., Eds.; Materials Research Society: Warrendale, PA, USA, 1999; pp 409–414.

(33) Ruthven, D. M.; Derrah, R. I. Diffusion of Monatomic and Diatomic Gases in 4A and 5A Zeolites. *J. Chem. Soc. Faraday Trans. 1 Phys. Chem. Condens. Phases* **1975**, *71*, 2031–2044.

(34) IZA Database of Zeolite Structures http://europe.iza-structure.org (accessed Nov, 2021).

(35) Wang, J. Y.; Mangano, E.; Brandani, S.; Ruthven, D. M. A Review of Common Practices in Gravimetric and Volumetric Adsorption Kinetic Experiments. *Adsorption* **2021**, *27*, 295–318.

(36) Thommes, M.; Kaneko, K.; Neimark, A. V.; Olivier, J. P.; Rodriguez-Reinoso, F.; Rouquerol, J.; Sing, K. S. W. W. Physisorption of Gases, with Special Reference to the Evaluation of Surface Area and Pore Size Distribution (IUPAC Technical Report). *Pure Appl. Chem.* **2015**, *87*, 1051–1069.

(37) Shang, J.; Li, G.; Singh, R.; Gu, Q.; Nairn, K. M.; Bastow, T. J.; Medhekar, N.; Doherty, C. M.; Hill, A. J.; Liu, J. Z. *et al*. Discriminative Separation of Gases by a "Molecular Trapdoor" Mechanism in Chabazite Zeolites. *J. Am. Chem. Soc.* **2012**, *134*, 19246–19253.

(38) Pirngruber, G. D.; Raybaud, P.; Belmabkhout, Y.; Čejka, J.; Zukal, A. The Role of the Extra-Framework Cations in the Adsorption of CO_2 on Faujasite Y. *Phys. Chem. Chem.*

Phys. **2010**, *12*, 13534–13546.

(39) Lozinska, M. M.; Miller, D. N.; Brandani, S.; Wright, P. A. Hiding Extra-Framework Cations in Zeolites L and Y by Internal Ion Exchange and Its Effect on CO_2 Adsorption. *J. Mater. Chem. A* **2020**, *8*, 3280–3292.